An ex vivo tumor fragment platform to dissect response to PD-1 blockade in cancer

Voabil, P.; Bruijn, M. de; Roelofsen, L.M.; Hendriks, S.H.; Brokamp, S.; Braber, M. van den; ... ; Thommen, D.S.

ARTICLES
https://doi.org/10.1038/s41591-021-01398-3

nature medicine

Check for updates

An ex vivo tumor fragment platform to dissect response to PD-1 blockade in cancer

Paula Voabil[1,9], Marjolein de Bruijn[2,9], Lisanne M. Roelofsen[2,9], Sanne H. Hendriks[2,7], Simone Brokamp[2], Marlous van den Braber[2,8], Annegien Broeks[3], Joyce Sanders[3], Petra Herzig[4], Alfred Zippelius[4], Christian U. Blank[2,5], Koen J. Hartemink[6], Kim Monkhorst[3], John B.A.G. Haanen[2,5], Ton N. Schumacher[1,10] and Daniela S. Thommen[2,10] ✉

Inhibitors of the PD-1–PD-L1 axis have been approved as therapy for many human cancers. In spite of the evidence for their widespread clinical activity, little is known about the immunological alterations that occur in human cancer tissue after PD-1 blockade. We developed and employed a patient-derived tumor fragment platform to dissect the early immunological response of human tumor tissue to ex vivo PD-1 blockade. We observed that the capacity of immune cells to be reactivated ex vivo was predictive of clinical response, and perturbation analyses identified tumor-resident T cells as a key component of this immunological response. In addition, through combined analysis of baseline properties and immune response capacity, we identified a new subgroup of infiltrated tumors that lacks the capacity to respond to PD-1 blockade. Finally, the baseline presence of tertiary lymphoid structures and their components correlated with the capacity of cancers to undergo intratumoral immune cell reactivation.

Immune checkpoint blockade targeting the PD-1–PD-L1 pathway has transformed cancer treatment in many tumor types. At present, PD-1 and/or PD-L1 blocking antibodies have been approved for 16 tumor types[1]. In addition, PD-1–PD-L1 blockade is the backbone of 1,000 of ongoing clinical studies that evaluate combination immunotherapies in oncology[1]. In spite of the central role of the PD-1–PD-L1 axis blockade in oncology, the immunological consequences of such a blockade in human cancers are incompletely understood. To provide three specific examples, recent data suggest that (1) PD-1 blockade may mainly target peripheral rather than tumor-resident T cells, as inferred from changes in the intratumoral T cell receptor (TCR) repertoire between pre- and on-treatment biopsies[2–4], (2) PD-1 blockade may, to a substantial extent, act via myeloid cells, as based on mouse models where PD-1 is selectively absent on such cells[5] and (3) PD-1 and PD-L1 blockade may not necessarily be functionally equivalent, as based on evidence in preclinical models indicating that the latter can free up a pool of B7 molecules on antigen-presenting cells (APCs) that may provide a costimulatory signal[6].

To assess how the immunological properties of human cancers are altered after PD-1 blockade, a number of studies have compared pre- and on-treatment biopsies to evaluate, for instance, changes in the abundance of defined T cell populations or changes in the intratumoral TCR repertoire[7,8]. While this approach is important to understand the longer-term consequences of immune checkpoint blockade, its value in deciphering the early effects of checkpoint blockade is limited. Notably, the observation of a 30% complete or major pathological response rate after a single cycle of anti-PD-1 in a recent neoadjuvant study in melanoma[9] underscores the importance of early changes in intratumoral immune activity. As a second limitation of current approaches, the use of serial biopsies does not allow one to directly compare the effects of different perturbations, complicating efforts to answer mechanistic questions.

Human ex vivo systems that maintain the tumor microenvironment (TME) and architecture as found in the patient, but that enable perturbation by immunotherapies, provide an opportunity to study both the dynamics of the treatment response and baseline properties of a tumor. In two recent studies, different technologies have been devised to investigate ex vivo responses to immune checkpoint blockade. In particular, a system using human air–liquid interface organoids consisting of both tumor and stroma components was shown to allow preservation of the intratumoral T cell repertoire and showed upregulation of interferon-γ (IFN-γ), granzyme B and perforin expression on PD-1 blockade[10]. Similarly, ex vivo treatment with anti-PD-1 and/or anti-CTLA-4 was shown to elicit cytokine secretion in patient-derived organotypic tumor spheroids[11]. However, a notable correlation between these immunological alterations and clinical response to immune checkpoint blockade was not established. The development of ex vivo models that can predict the clinical response would be of particular value since it would allow one to assess the effect of additional perturbations on the TME and thereby directly test the functional importance of specific cell types or cytokines in the treatment response. Toward this goal, we developed and validated a patient-derived tumor fragment (PDTF) platform to assess the early immunological response of five different cancer types to ex vivo PD-1 blockade. We subsequently

[1]Division of Molecular Oncology & Immunology, Oncode Institute, Netherlands Cancer Institute, Amsterdam, the Netherlands. [2]Division of Molecular Oncology & Immunology, Netherlands Cancer Institute, Amsterdam, the Netherlands. [3]Department of Pathology, Netherlands Cancer Institute, Amsterdam, the Netherlands. [4]Department of Biomedicine, University Hospital Basel, Basel, Switzerland. [5]Department of Medical Oncology, Netherlands Cancer Institute, Amsterdam, the Netherlands. [6]Department of Surgery, Netherlands Cancer Institute, Amsterdam, the Netherlands. [7]Present address: Department of Immunohematology and Blood Transfusion, Leiden University Medical Center, Leiden, the Netherlands. [8]Present address: Department of Molecular Cell Biology and Immunology, Amsterdam University Medical Center, Vrije Universiteit Amsterdam, Amsterdam, the Netherlands. [9]These authors contributed equally: Paula Voabil, Marjolein de Bruijn, Lisanne M. Roelofsen. [10]These authors jointly supervised this work: Ton N. Schumacher, Daniela S. Thommen. ✉e-mail: d.thommen@nki.nl

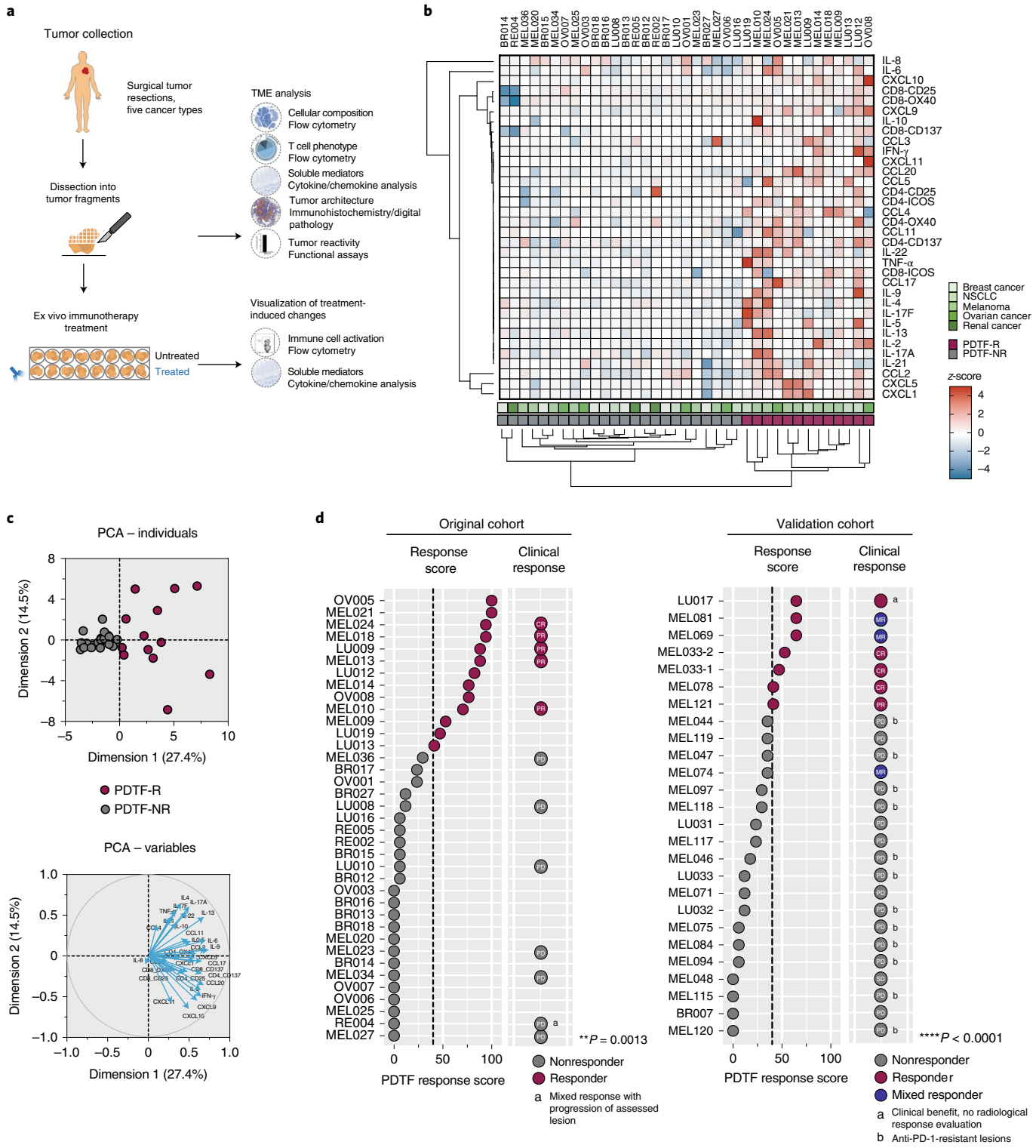

Fig. 1 | A human tumor fragment platform that responds to PD-1 blockade. a, Schematic representation of PDTF collection, culture and analysis strategy. **b**, Heatmap displaying normalized delta values between the anti-PD-1 treated and untreated conditions for each parameter (4 T cell activation markers, 13 cytokines, 13 chemokines, $n = 37$ tumors; Supplementary Table 1). Unsupervised hierarchical clustering identified two large groups, subsequently termed PDTF-R and PDTF-NR. **c**, PCA of the data in **b**, showing the separation of samples (top) and parameters (bottom). **d**, PDTF response score (as defined in Extended Data Fig. 4) for each tumor and matched clinical response for tumors from patients treated with PD-1 blockade. CR, complete response; PR, partial response; SD, stable disease; PD, progressive disease. The graph on the left shows the original cohort ($n = 37$), the graph on the right shows a validation cohort ($n = 26$; Supplementary Table 2) with matched clinical data. anti-PD-1-resistant tumors indicate the PDTF responses of progressive lesions from patients who received systemic anti-PD-1 treatment before the lesion was surgically removed. Significance was determined by two-sided Fisher's exact test.

used this platform to evaluate (1) whether the early immunological response correlates with the clinical response, (2) whether there are baseline parameters that can predict immunological responsiveness and (3) whether distinct subtypes of immunologically nonresponsive tumors can be identified. Our data demonstrate that the capacity of tumors to respond clinically to PD-1 blockade correlates with the capacity of already resident intratumoral immune cells to be reactivated by the PD-1 pathway blockade. Furthermore, this immunological responsiveness is driven, at least in part, by preexisting intratumoral T cells. In addition, we identified three subtypes of nonresponsive tumors that differ in both the magnitude and location of the T cell infiltrate but share a lack of substantial tumor reactivity. Finally, the baseline presence of tertiary lymphoid structures (TLS) and their components were predictive of the capacity of cancers to undergo immune cell reactivation after PD-1 blockade.

Results

A human tumor fragment platform that preserves TME and architecture. To assess the early immunological responses of human cancers to PD-1 blockade, we developed an organotypic culture platform using PDTFs (Fig. 1a). In this platform, fresh tumor tissue from surgical resections was dissected into fragments of approximately 1 mm^3, with the aim to allow sufficient nutrient and reagent access while preserving the cellular contexture and architecture of the tumor. Furthermore, the use of small-sized tumor fragments also allows the mixing of PDTFs from different tumor areas, thereby reducing the confounding effects of tumor heterogeneity (Extended Data Fig. 1a). To prevent immune cell efflux, PDTFs were embedded into an artificial extracellular matrix (Extended Data Fig. 1b,c). To assess the stability of the tissue during culture, T cell, non-T cell and nonimmune cell compartments, as well as cytokine and chemokine secretion, were analyzed at different time points. Stable levels of cellular and soluble factors were observed up to 48 h of culture ($n=4$), indicating that this system allows the analysis of early effects of ex vivo treatment (Extended Data Fig. 1d). By comparing PDTF cultures with and without matrix, we confirmed that embedding in matrix did not limit T cell functionality or induce unspecific immune activation (Supplementary Fig. 1a–d). Penetration of exogenously added antibodies into PDTFs was validated by both flow cytometry and immunofluorescence staining (Extended Data Fig. 1f); parallel cultures of PDTFs from six tumors showed comparable patterns of steady-state secretion of soluble factors for all matched samples, providing a measure of the reproducibility of the data obtained (Extended Data Fig. 1e). Jointly, these and additional data (Supplementary Fig. 1e–h) validate PDTFs as a platform to assess the functional importance of certain cell types or cytokines after ex vivo immunotherapeutic perturbation.

Immunological response of human cancers to PD-1 blockade. To evaluate the immunological response to PD-1 blockade in distinct human cancers (relevant controls shown in Extended Data Fig. 2a–c), we profiled the effect of PD-1 blockade on 37 tumors from five different cancer types (melanoma, non-small cell lung cancer (NSCLC), breast cancer, ovarian cancer and renal cell carcinoma) (Extended Data Fig. 2d), using 13 cytokines, 13 chemokines and 4 T cell activation markers as readouts. For each parameter, normalized delta values between the anti-PD-1-treated and untreated conditions were determined and used for unsupervised hierarchical clustering. This analysis revealed two broad groups of tumors: a larger group that showed only minor treatment-induced changes in all of the assessed parameters (24 out of 37 tumors, hereafter referred to as PDTF nonresponders (PDTF-NRs)), and a smaller group of tumors (13 out of 37) that displayed a clear increase in immune activity after ex vivo PD-1 blockade (PDTF responders, (PDTF-Rs)) (Fig. 1b). The immunological responder group was dominated by melanoma and NSCLC samples but also contained two ovarian cancers. Principal component analysis (PCA) resulted in a similar division between PDTF-NR and PDTF-R samples and indicated a further subdivision of PDTF-R tumors based on distinct response patterns (Fig. 1c). While response patterns were reproducible in independent PDTF cultures from the same tumor (Extended Data Fig. 3a), analysis of individual tumor fragments, rather than pooled tumor fragments, demonstrated intratumoral heterogeneity in response capacity (Extended Data Fig. 3b,c). Modeling of these data emphasized the need to average PDTF responses over a series of approximately eight tumor fragments (Extended Data Fig. 3d), as done in all standard PDTF cultures.

Area under the curve (AUC) analysis of individual parameters revealed that the separation of PDTF-R and PDTF-NR tumors was mostly driven by a subset of parameters, including CXCL1, IFN-γ and CXCL10 (see below) and this information was used to establish a PDTF response score based on the most discriminative parameters (Extended Data Fig. 4a–c). To understand whether these ex vivo immunological responses of resected lesions would correlate with clinical response, we focused on the 12 patients who subsequently received PD-1 blocking therapy. Even though immunological response was in some cases assessed on lesions that were resected during an earlier disease stage, ex vivo PDTF response and clinical response correlated in 12 out of 12 cases ($P=0.0013$; Fig. 1d, clinical response reflects best radiological response). To further understand the relationship between ex vivo PDTF response and clinical response, an additional cohort of 26 patients with matched clinical response data, including melanoma and NSCLC lesions obtained from 12 patients who did not respond to clinical PD-1 blockade, was assessed. For the three patients experiencing a mixed response, an immunological response was observed in two out of three cases. For the 23 patients achieving either a partial or complete response ($n=5$) or showing stable or progressive disease ($n=18$), clinical outcomes were in all cases in full concordance with the immunological response ($P<0.0001$) (Fig. 1d). To understand whether different tumor lesions of a patient show heterogeneity in their immunological response, we assessed ex vivo anti-PD-1 responses

Fig. 2 | Tumor-resident T cells promote response to PD-1 blockade. a, Quantification of activation markers on $CD3^+$ T cells and secreted T cell effector cytokines in PDTFs in the absence or presence of ex vivo PD-1 blockade, as assessed by flow cytometry and bead-based immunoassay, respectively. Shown is an example of a representative responding tumor sample (LU012). **b**, Cytotoxic markers secreted by untreated and anti-PD-1-treated PDTFs displayed separately for PDTF-R and PDTF-NR ($n=30$, same experiment as in Fig. 1b). $^*P<0.05$, $^{**}P<0.01$ by two-tailed Wilcoxon test. **c**, Heatmap displaying normalized delta values between the anti-PD-1-treated and untreated condition for each cytotoxic marker. **d**, Effect sizes (calculated as Hedge's *g*) and *P* values (by two-tailed Mann–Whitney *U*-test) of normalized changes for all cytokine and chemokine parameters and activation markers assessed. **e**, Most significantly increased parameters between untreated and anti-PD-1 treated PDTFs displayed separately for PDTF-R and PDTF-NR. $^*P<0.05$, $^{**}P<0.01$, $^{***}P<0.001$ by two-tailed Wilcoxon test. **f**, Correlation of $\log_2$ fold changes (to untreated control) of either two independent PDTF cultures treated with anti-PD-1 (left) or of PDTF cultures treated with anti-PD-1 in the absence or presence of IFN-γR1 blocking antibody (aIFNγR1, middle), or LCK inhibitor (LCKi, right), respectively. **g**, Correlation of normalized values (*z*-score) of PDTF cultures that were either untreated or treated with anti-PD-1 + LCKi. **h**, Heatmap showing the normalized values of parameters that decreased below steady-state levels in the presence of LCK inhibitor. Note that while we formally cannot exclude an effect through inhibition of LCK in NK/NKT cells, this is considered unlikely because of their low frequencies (150-fold lower than T cells in PDTF-R).

in PDTFs from 11 patients for whom multiple lesions could be collected. Of note, in 8 out of 11 (73%) patients, we observed concordant immunological responses (Extended Data Fig. 4d). Most samples in our cohort were derived from primary tumor lesions (Extended Data Fig. 2d and Supplementary Table 1) and the PDTF-R group showed a slight enrichment for lymph node

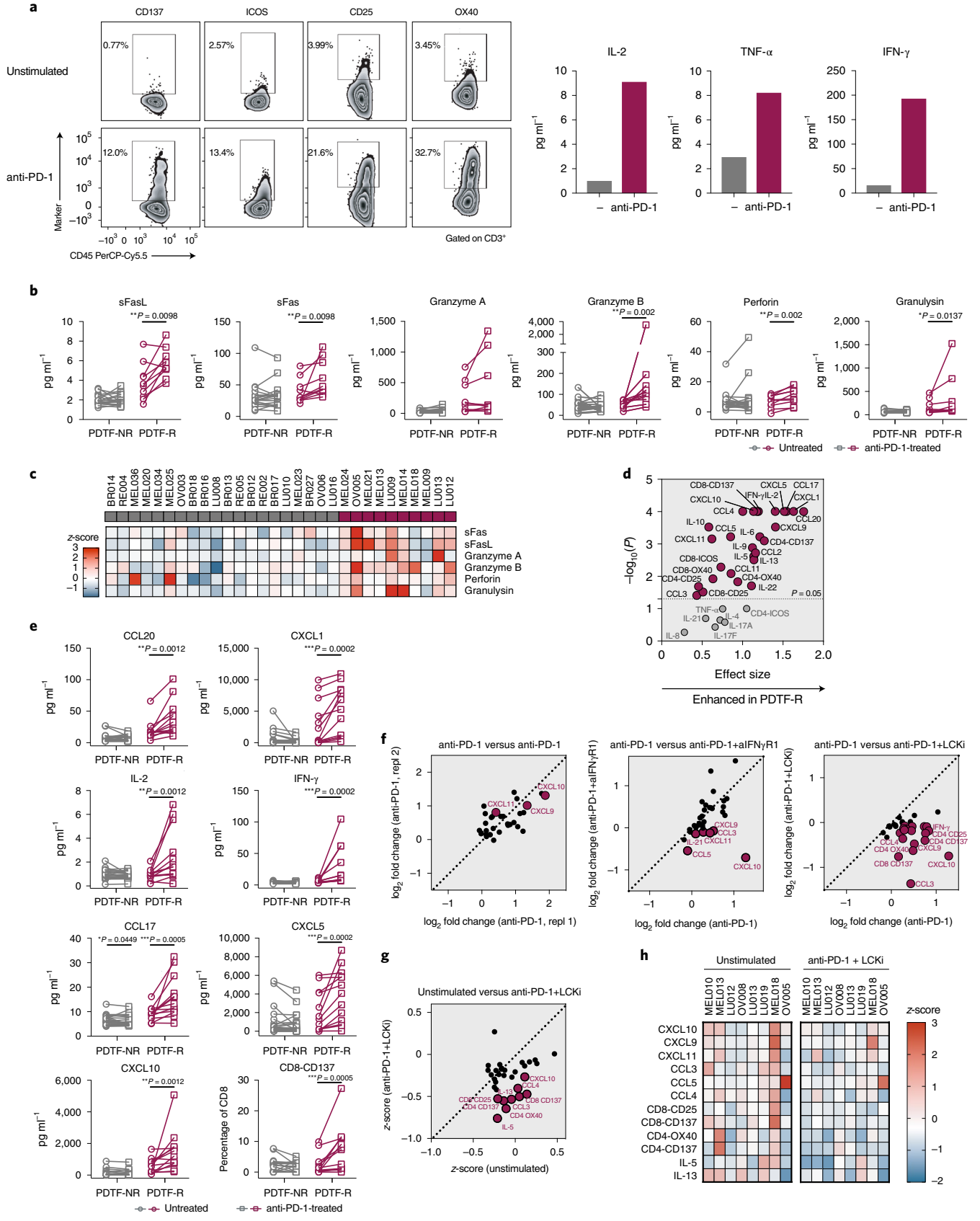

metastases (4 out of 13 compared to 4 out of 24 PDTF-NRs). To determine whether the immunological responses observed were mainly driven by lymph node metastases, anti-PD-1 responses in PDTFs from 27 lymph node metastases and 18 lesions of primary tumors or distant metastases were compared, showing similar ranges of the response score between the two groups (Extended Data Fig. 4e). Jointly, the above data indicate that clinical response to anti-PD-1 therapy correlates with the capacity of tumor-resident immune cells to be (re)activated by PD-1–PD-L1 pathway blockade.

Tumor-resident T cells drive the response to PD-1 blockade. Previous work provided evidence for a role of T cells in the activity of PD-1 blocking antibodies[12] and the high-level expression of PD-1 on human tumor-reactive T cells is in line with this model[13–15]. However, it is presently unclear whether tumor-resident T cells can be reactivated by PD-1 blockade or whether treatment mainly mobilizes peripheral T cells as suggested recently[2,3]. Analysis of T cell activation markers, as well as the T cell effector cytokines interleukin-2 (IL-2), tumor necrosis factor-α (TNF-α) and IFN-γ, revealed detectable increases after ex vivo PD-1 blockade in PDTF-R tumors (Fig. 2a and Extended Data Fig. 5a). Importantly, tumor-resident T cells in PDTF-NR tumors did not respond to PD-1 blockade but could be activated by anti-CD3 antibodies (Extended Data Fig. 5b,c), indicating that these T cells can respond to TCR triggering and that the PD-1–PD-L1 axis is not a critical signaling pathway that limits the physiological activity of this T cell pool. PD-1 blockade further induced the release of multiple cytotoxicity markers including perforin, granzymes A and B and granulysin in PDTF-R tumors, which is suggestive of reactivation of an intratumoral cytotoxic T or natural killer (NK) cell response (Fig. 2b,c). Importantly, not only parameters that directly reflect T cell activation, such as CD137 expression and IL-2 and IFN-γ production, but also IFN-γ target molecules, such as the CXCL9 and CXCL10 chemokines, were increased by PD-1 blockade. In addition, induction of a series of other chemokines, including CXCL1, CXCL5, CCL17 and CCL20, was significantly associated with response (Fig. 2d,e and Extended Data Fig. 6).

Recent work from Strauss et al.[5] has provided clear evidence that PD-1 blockade may not only act on T cells but that PD-1 expression on myeloid cells may contribute substantially to the activity of PD-1 blocking therapies in mouse models[5]. To understand to what extent the observed immune reactivation in human cancers could be modulated by either preventing TCR signaling or downstream IFN-γ receptor signaling, we pretreated PDTFs from eight responding tumors with either a lymphocyte-specific protein tyrosine kinase inhibitor (LCKi) or with an IFNγR1 blocking antibody (aIFNγR1, optimal concentrations identified by titration experiments using anti-CD3/anti-CD28-stimulated peripheral blood mononuclear cells (PBMCs); Extended Data Fig. 7a–c). Preincubation of PDTFs with aIFNγR1 antibody abolished part of the anti-PD-1 response, with the most profound effects on IFN-γ-induced molecules, such as CXCL9, CXCL10 and CXCL11, on $CD4^+$ T cell cytokines, such as IL-21, as well as on the chemokines CCL3 and CCL5 (Fig. 2f and Extended Data Fig. 7d,e). Notably, inclusion of LCKi prevented anti-PD-1-induced immune reactivation for most parameters (Fig. 2f and Extended Data Fig. 7d,e). In addition, LCK inhibition in PDTF-R tumors not only abolished immune activity after PD-1 blockade but reduced immune activity below the levels present during steady state (Fig. 2g,h and Extended Data Fig. 7d,e). Jointly, these data provide evidence that immune reactivation after PD-1 blockade is to a large part dependent on tumor-resident T cells. In addition, the data suggest that the T cell pool in these tumors is generally not fully inert before PD-1 blockade but is characterized by a low-level steady-state antitumor response.

Subtypes of immunologically nonresponsive tumors. Having established that preexisting immune cells can be reactivated in only part of human tumors, we wished to explore whether the baseline properties of tumors can predict capacity for immune reactivation by PD-1 blockade. Previous studies indicated that the level and type of immune infiltrate of human tumors are associated with clinical response to immunotherapy[16–19]. Jointly, these studies have led to the definition of three major tumor subgroups: immune desert tumors where immune cells are largely absent; excluded tumors where the T cell compartment is primarily peritumoral; and infiltrated tumors where the T cell infiltrate is observed among tumor cell nests. To investigate whether the differences in the observed immunological response of human cancers to PD-1 blockade could be explained by distinct immune contextures, we first quantified immune cell fractions by flow cytometry (Extended Data Fig. 8a). This revealed a subgroup of tumors (10 out of 37, 27%) that lacked a substantial immune compartment (<10% immune cells). In line with expectations, 0 out of 10 of these tumors had been identified as PDTF-R (Fig. 3a,b). Among the remaining 27 tumors, an immune cell compartment of comparable magnitude was observed for nonresponding and responding tumors, with an enrichment in B cells in the latter (Fig. 3a and Extended Data Fig. 8b; see below). To understand whether the presence of $CD8^+$ T cells either inside or outside of tumor cell nests could be used to further identify tumors that respond to PD-1 blockade, we performed digital image analysis of $CD8^+$ T cells in tumor and stromal areas (Fig. 3c and Extended Data Fig. 8c). While $CD8^+$ T cells were generally more abundant in stromal areas and total numbers differed across cancer types (Extended Data Fig. 8d), distinct spatial patterns could be identified. Importantly, within the immune cell-rich tumors ($n=26$, no immunohistochemistry (IHC) data were available for BR015), this analysis identified 7 tumors with an excluded $CD8^+$ T cell pool, where $CD8^+$ cells were present in stromal areas but not or at very low numbers within tumor regions. Notably, six out of seven of these tumors did not show immune reactivation after PD-1 blockade (Fig. 3c). Thus, of the tumors that were characterized as either immune deserts or as $CD8^+$ T cell-excluded, only 1 out of 17 (5.9%) showed immune cell reactivation after ex vivo PD-1 blockade, potentially explaining the low clinical response rates previously

Fig. 3 | Baseline tumor properties and correlation with immunological response. a, Quantification of major immune subsets within total live cells by flow cytometry. **b**, Quantification of immune infiltrates ($CD45^+$) in immune deserts, immune cell-rich nonresponding and immune cell-rich responding tumors ($n=37$ tumors). Shown are the mean ± s.d.; $^{**}P<0.01$, $^{****}P<0.0001$ by Kruskal–Wallis test corrected for multiple comparisons. NS, not significant. **c**, Strategy for algorithm-based digital area quantification (left) and examples of the two $CD8^+$ T cell distribution patterns observed in immune cell-rich tumors (middle). The pie charts indicate the fractions of responding and nonresponding tumors in excluded and infiltrated TMEs, respectively. **d**, Heatmap of steady-state cytokine and chemokine levels. The data depict normalized values measured after 48 h of untreated PDTF culture. Unsupervised clustering was performed within the four defined TME types (desert, excluded, infiltrated PDTF-NR, infiltrated PDTF-R). **e**, Quantification of total steady-state cytokine/chemokine secretion, depicted as the sum of all normalized parameters ($n=37$ tumors). Shown are the mean ± s.d., $^{*}P<0.05$, $^{**}P<0.01$ by Kruskal–Wallis test corrected for multiple comparisons. **f**, Effect sizes (calculated by Hedge's g) and P values (by two-tailed Mann–Whitney U-test) of steady-state cytokines and chemokines between PDTF-R and PDTF-NR. **g**, Quantification of the three parameters with the highest statistical significance and largest effect size in the distinct TME subtypes ($n=37$ tumors). Shown are the mean ± s.d.; $^{*}P<0.05$, $^{**}P<0.01$, $^{***}P<0.001$ by Kruskal–Wallis test corrected for multiple comparisons.

observed in tumors with such microenvironments[7,16]. In contrast, immune cell reactivation after PD-1 blockade was observed in 12 out of 19 CD8+ infiltrated tumors.

To understand the basis for differences in immunological response capacity within the final subgroup of CD8+-infiltrated tumors, we classified the PDTF cohort into four TME

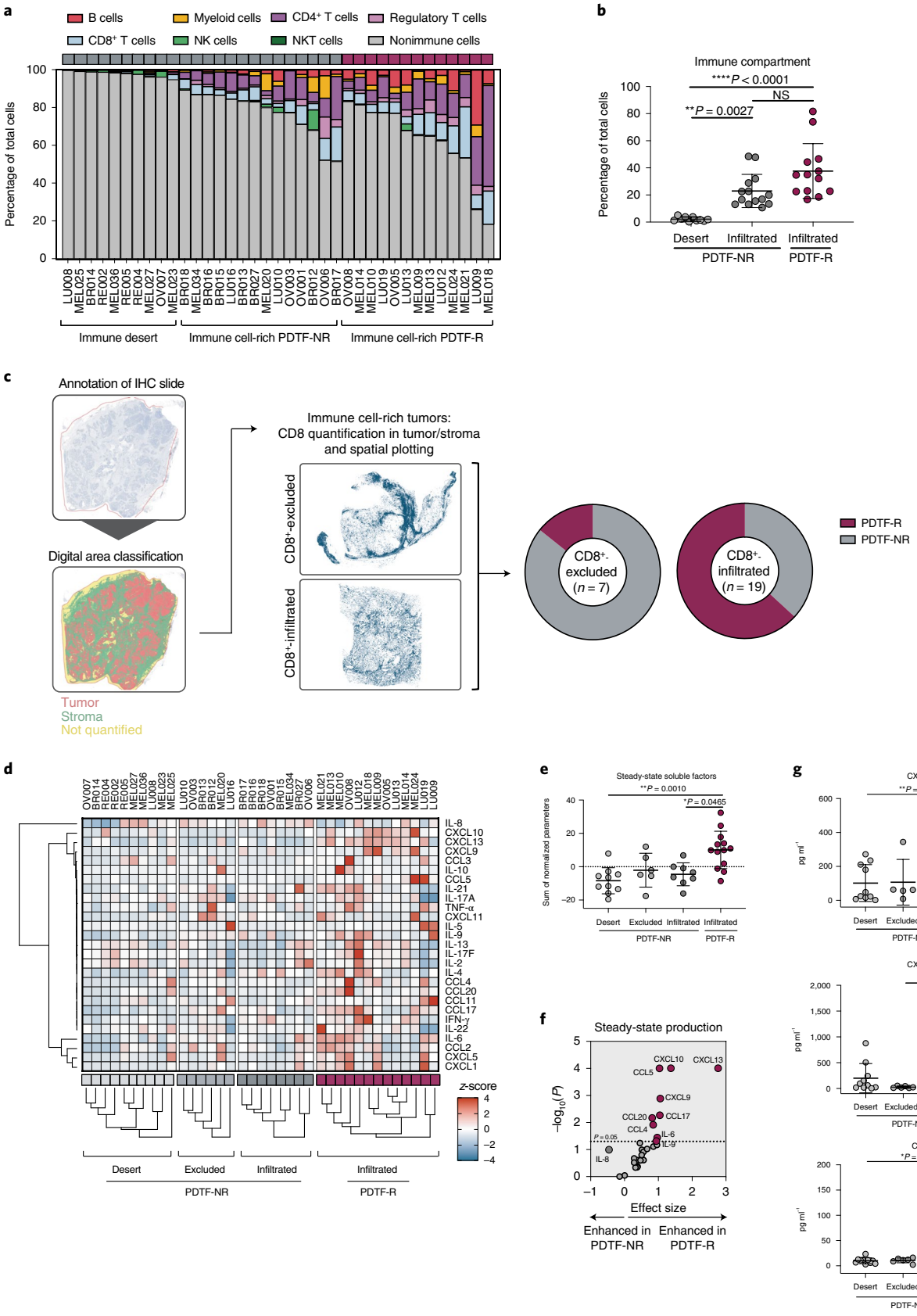

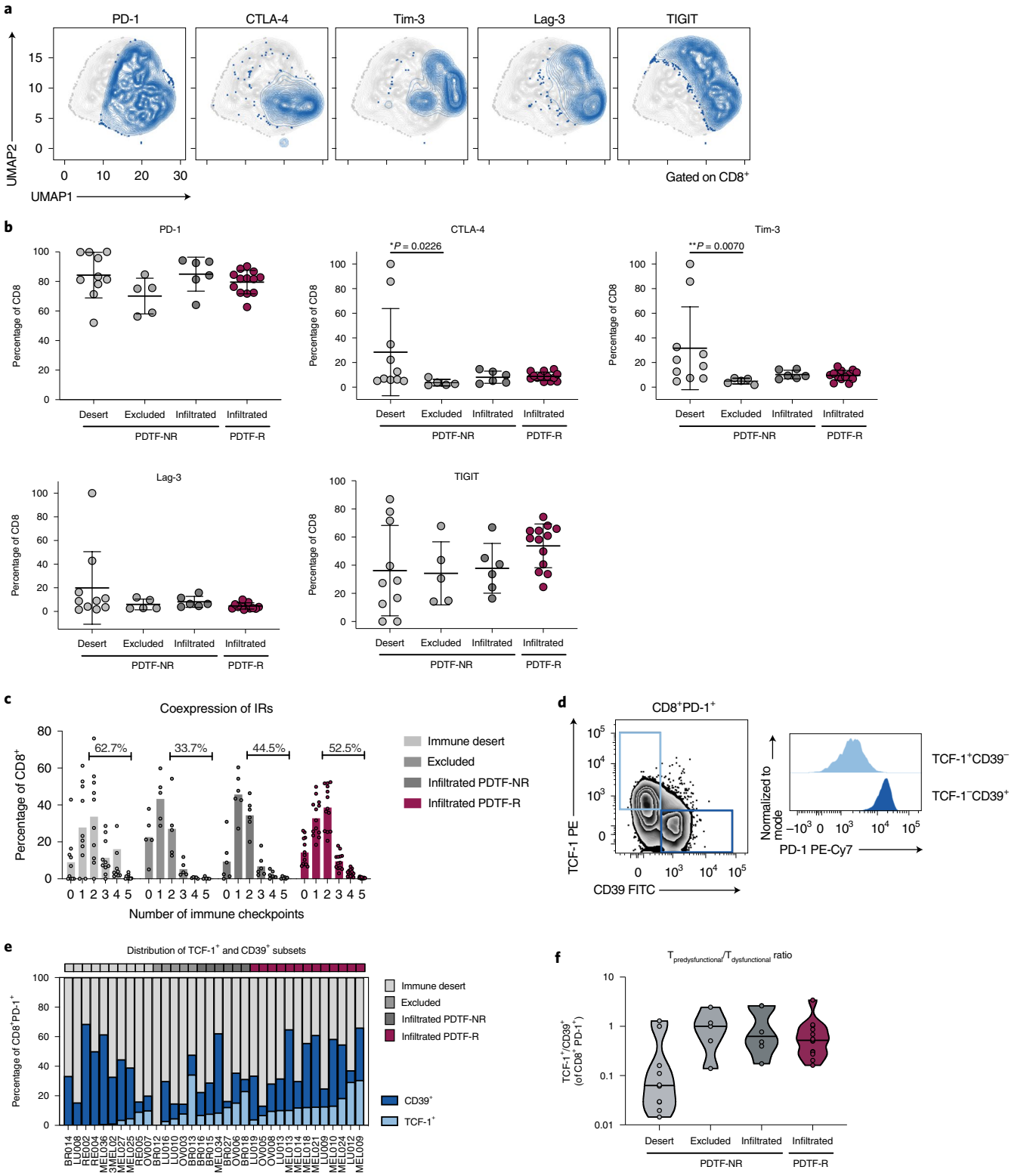

Fig. 4 | T cell differentiation states across distinct TME types. a, Uniform manifold approximation and projection (UMAP) plots of CD8⁺ T cells concatenated and equalized from all tumors analyzed ($n = 34$) showing the expression of the indicated immune checkpoints. **b**, Percentage of CD8⁺ T cells expressing the indicated inhibitory receptors within the distinct TME subtypes ($n = 34$ tumors). Shown are the mean ± s.d.; $^{*}P < 0.05$, $^{**}P < 0.01$ by Kruskal–Wallis test corrected for multiple comparisons. **c**, Percentage of CD8⁺ T cells expressing none or 1–5 immune checkpoints, as determined by Boolean gating within the distinct TME subtypes ($n = 34$ tumors). The bars indicate the mean. The numbers reflect the fraction of CD8⁺ T cells coexpressing ≥ 2 markers. **d**, Flow cytometry analysis showing the expression of TCF-1 and CD39 within PD-1⁺CD8⁺ T cells to identify predysfunctional (TCF-1⁺CD39⁻) and dysfunctional subsets (TCF-1⁻CD39⁺), respectively (left). Right: histograms depicting the PD-1 expression level within the two populations indicated in the left plot. **e**, Distribution of TCF-1⁺ and CD39⁺ subsets within the CD8⁺PD-1⁺ T cell population for each tumor in the four different TME subtypes. **f**, Ratio of TCF-1⁺ and CD39⁺ cells within PD-1⁺ CD8⁺ T cells in the distinct TME subtypes.

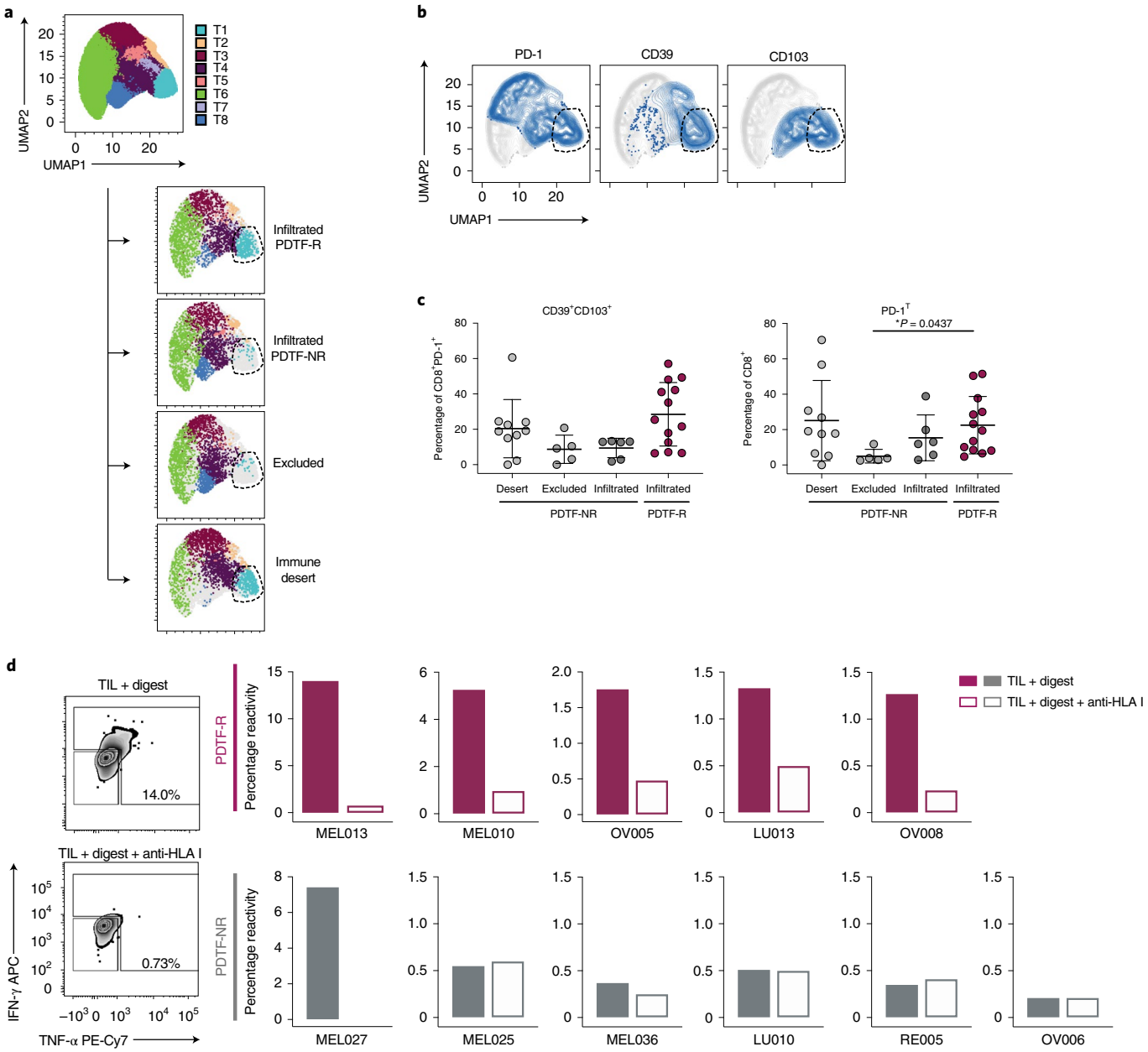

Fig. 5 | Differential tumor reactivity in T cell populations in PDTF-R and PDTF-NR tumors. a, UMAP plots of CD8⁺ T cells in distinct TME subtypes. CD8⁺ T cells from all tumors analyzed ($n = 34$) were concatenated and the PD-1⁺ subset was normalized to 1,600 cells per TME subtype. Clusters reflect subsets with distinct expression of PD-1, CD39, CD103 and TCF-1 (Extended data Fig. 10e). T1 (indicated by the dashed line) marks the cluster expressing markers associated with tumor reactivity. **b**, Overlay of PD-1, CD39 and CD103 on the UMAP plot. **c**, Quantification of CD39⁺CD103⁺ cells within CD8⁺PD-1⁺ T cells or of PD-1^T cells within CD8⁺ T cells across the distinct TME subtypes ($n = 34$ tumors). PD-1^T expression is defined as a PD-1 expression level above the level found on peripheral blood CD8⁺ T cells, as described previously[15]. Shown are the mean ± s.d.; $^*P < 0.05$ by Kruskal–Wallis test corrected for multiple comparisons. **d**, Representative flow cytometry plots depicting IFN-γ and TNF-α production on coculture of expanded CD8⁺ T cells (TILs) with autologous tumor digest in the absence or presence of an HLA class I blocking antibody (left). Tumor reactivity is defined as the production of either IFN-γ, TNF-α or both cytokines. Right: percentage of CD8⁺ reactivity in the absence or presence of HLA class I blocking antibody in five PDTF-R and six PDTF-NR tumors.

types—immune deserts, CD8⁺-excluded, CD8⁺-infiltrated PDTF-NR and CD8⁺-infiltrated PDTF-R tumors. Subsequently, we compared these groups with respect to four different properties: (1) the presence of a baseline inflammatory signature; (2) the differentiation states of tumor-resident myeloid cells and T cells; (3) the presence of a tumor-reactive T cell compartment; and (4) the evidence for the formation of TLS.

Baseline chemokine production and immune cell states across TME types. Analysis of cytokine and chemokine production after 48 h of PDTF culture without treatment revealed heightened baseline activity in PDTF-R tumors, not only when compared to immune desert tumors and CD8⁺-excluded tumors, but also when compared to CD8⁺-infiltrated PDTF-NR tumors (Fig. 3d,e, Extended data Fig. 9 and Supplementary Fig. 2). Parameters for which baseline

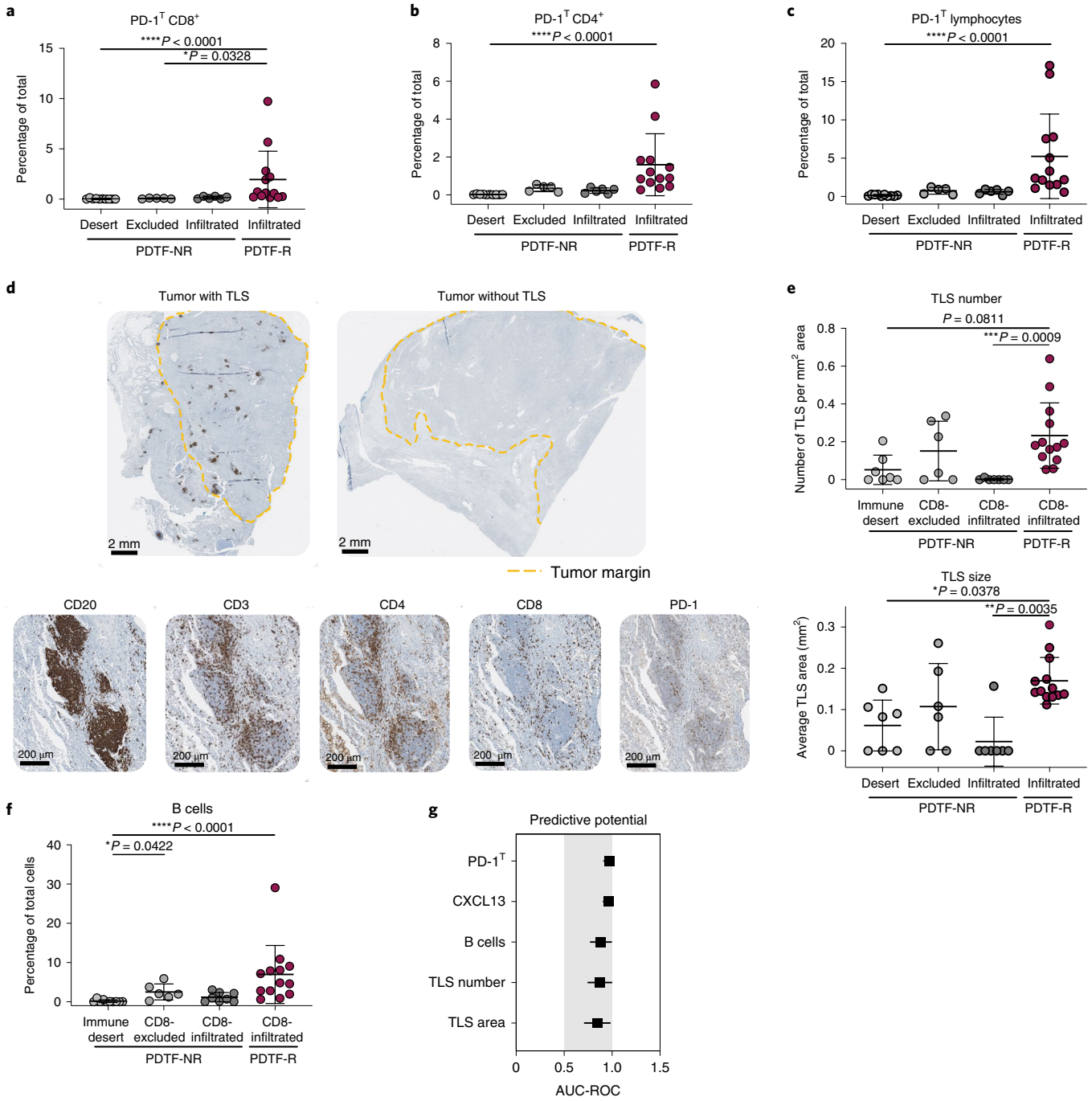

Fig. 6 | TLS and their components predict the capacity of human tumors to respond to PD-1 blockade. a–**c**, Frequency of PD-1^{T}CD8^{+} T cells (**a**), PD-1^{T}CD4^{+} T cells (**b**) and PD-1^{T}CD45^{+} lymphocytes (**c**) within total cells across TME subtypes ($n = 34$ tumors). Shown are the mean ± s.d., $^{*}P < 0.05$, $^{****}P < 0.0001$ by Kruskal–Wallis test corrected for multiple comparisons. **d**, Example of two tumors out of 33 analyzed, one containing TLS (OV008, top left) and one lacking TLS (RE002, top right). TLS are indicated by CD20 staining. IHC staining of the indicated markers in TLS (bottom). Shown is a region with representative TLS in a lung cancer sample (LU009). **e**, Number and average size of TLS in distinct TME subtypes ($n = 33$ tumors). TLS were identified by CD20 and CD3 staining and quantified and measured by digital analysis. Lymphoid aggregates < 60,000 µm^{2} were excluded, as described previously[42]. Shown are the mean ± s.d.; $^{*}P < 0.05$, $^{**}P < 0.01$, $^{***}P < 0.001$ by Kruskal–Wallis test corrected for multiple comparisons. **f**, Quantification of B cells within total live cells across TME subtypes ($n = 37$ tumors). Shown are mean ± s.d.; $^{*}P < 0.05$, $^{****}P < 0.001$ by Kruskal–Wallis test corrected for multiple comparisons. **g**, Predictive potential of indicated markers defined by the AUC-ROC.

production predicted capacity for immune reactivation by PD-1 blockade included molecules such as CXCL9 and CXCL10 that may reflect low-level baseline T cell activity but also the chemokine CXCL13, which is associated with the formation of TLS (Fig. 3f,g and Extended Data Fig. 9). In addition, high IL-8 secretion showed a trend toward association with anti-PD-1 nonresponsiveness, in particular in infiltrated PDTF-NR (Fig. 3f, Extended Data Fig. 9 and Supplementary Fig. 2), an observation that deserves follow-up in view of previous data documenting increased serum IL-8 levels in nonresponders to immune checkpoint blockade[20–22].

To understand whether the TME groups differed with regard to the cell states of infiltrating myeloid and T cell populations, we assessed both cell populations by flow cytometry. The immune infiltrate in PDTF-R tumors generally contained fewer myeloid cells, particularly compared to infiltrated PDTF-NR and immune desert tumors (Supplementary Fig. 3a). An exploratory analysis of the composition of the myeloid cell pool revealed substantial variation across tumors (Supplementary Fig. 3b–e). While different frequencies of specific myeloid cell subsets were observed across TME subgroups, no subsets that were unique or predominant in a microenvironment were observed (Supplementary Fig. 3f,g). Since persistent antigen stimulation and immunosuppressive stimuli in the TME can induce a progressive dysfunctional state in T cells, which is accompanied by overexpression of multiple immune checkpoints[23–25], we next examined whether the expression of inhibitory receptors may predict capacity for immune reactivation after PD-1 blockade. To this end, we assessed expression of PD-1, CTLA-4, Tim-3, Lag-3 and T cell immunoreceptor with Ig and ITIM domains (TIGIT) on CD8$^+$ T cells (Fig. 4a). No significant difference in the fraction of inhibitory receptor-positive cells was observed between PDTF-Rs and infiltrated or excluded PDTF-NRs, except for a trend toward more frequent TIGIT expression in PDTF-R tumors. Surprisingly, immune deserts stood out by the frequent very high expression of several immune checkpoints on the few T cells present (Fig. 4b). In addition, immune deserts harbored the largest fraction of CD8$^+$ T cells that showed coexpression of multiple immune checkpoints (Fig. 4c and Extended Data Fig. 10a).

Recent data in murine cancer models and human melanoma[26–29] indicate that the dysfunctional T cell pool can be further subdivided into a progenitor or predysfunctional population that is characterized by the expression of the transcription factor TCF-1, and a more differentiated, dysfunctional population that is TCF-1$^-$ but expresses CD39. Importantly, the TCF-1$^+$ predysfunctional subset is essential for durable responses to immunotherapy in mouse models[26–28] and in patients undergoing adoptive T cell therapy[30]. To understand whether a difference in predysfunctional and dysfunctional subsets exists between PDTF-R and PDTF-NR tumors, we quantified TCF-1$^+$ and CD39$^+$ cells within the PD-1$^+$CD8$^+$ T cell pool. In line with previous data, TCF-1 was expressed in a subset of T cells that showed an intermediate PD-1 expression level and was mostly negative for CD39. In contrast, the CD39$^+$ subset was largely TCF-1$^-$ and expressed PD-1 at a very high level (Fig. 4d). The TCF-1$^+$ predysfunctional population could be identified in excluded and infiltrated TME types without a difference between responding and nonresponding tumors (Fig. 4e and Extended Data Fig. 10b). However, the balance between the predysfunctional and dysfunctional subset was strongly skewed toward the latter in immune deserts, indicating that the predysfunctional pool may be lacking in part of these tumors (Fig. 4e,f and Extended Data Fig. 10b,c).

Tumor reactivity varies in responding and nonresponding tumors. The coexpression of CD39 and CD103 has been shown to identify tumor-reactive T cells in solid tumors[31]. Similarly, CD8$^+$ T cells with a PD-1 expression level that exceeds that found in peripheral blood T cells, so-called PD-1^T tumor-infiltrating T lymphocytes (TILs), have been shown to display an enhanced capacity for tumor recognition in NSCLC[15]. To understand whether the prevalence of these T cell subsets may correlate with the capacity for immunological response to PD-1 blockade, we quantified CD39$^+$CD103$^+$ and PD-1^T CD8$^+$ T cell subsets in the different TME subgroups (Fig. 5a,b and Extended Data Fig. 10c–e). Notably, while expression of the tissue residency marker CD103 alone, which has been associated with response to PD-1 blockade according to previous studies[32–34], was comparable between TME subgroups (Extended Data Fig. 10d), the fraction of CD39$^+$CD103$^+$ double-positive cells was highest within CD8$^+$ T cells in PDTF-R and immune desert tumors; a similar observation was made for PD-1^T TILs (Fig. 5c; for absolute numbers, see below). To directly test for the presence of a tumor-specific T cell pool, CD3$^+$ TILs from five PDTF-R and six PDTF-NR tumors were sorted and expanded and tumor reactivity was determined by coculture with autologous tumor digests (Fig. 5d and controls in Extended Data Fig. 10f). Notably, in all TILs obtained from PDTF-R tumors, tumor reactivity among CD8$^+$ TILs was detected and tumor reactivity among CD4$^+$ TILs was detected in four out of five cases. In PDTF-NR tumors, tumor reactivity among CD8$^+$ TILs and CD4$^+$ TILs were both detected for only one out of six tumors (Fig. 5d and Extended Data Fig. 10g).

TLS and their components are predictive for response to PD-1 blockade. Jointly, the above analyses indicate that the capacity of a tumor to respond to PD-1 blockade may be related both to the magnitude of the T cell infiltrate and to the frequency of T cells with phenotypic characteristics of tumor-reactive T cells, such as high PD-1 expression or CD39/CD103 coexpression. Based on these two separate observations, we subsequently explored the predictive value of the absolute number of PD-1^T TILs, thereby combining the quantity and quality of tumor-resident T cells in a single metric. Both PD-1^{T}CD8$^+$ T cells, PD-1^{T}CD4$^+$ T cells and total PD-1^{T}CD45$^+$ lymphocytes were increased in responding tumors (Fig. 6a–c), with PD-1^T lymphocytes showing the best discrimination between PDTF-R and all other TME types independent of cancer type. Previous work established two characteristics of PD-1^T TILs that link these cells to TLS. First, PD-1^T TILs constitutively produce CXCL13, which is a crucial chemoattractant for the formation of TLS[35]. Second, in human NSCLC, PD-1^T TILs are predominantly localized within TLS[15]. Therefore, we subsequently assessed whether the presence of TLS or their components was associated with the capacity of a tumor to respond to PD-1 blockade. Quantification of TLS in PDTF-R and PDTF-NR tumors by CD20 and CD3 staining (Fig. 6d) revealed that both TLS number and size (defined as the average TLS area) were significantly higher in PDTF-R tumors, especially when compared to infiltrated PDTF-NR tumors (Fig. 6e). Notably, B cells, which are a major component of TLS, were also significantly enriched in PDTF-R tumors (Fig. 6f). To compare the potential of all parameters assessed in this study to predict the capacity of the intratumoral immune compartment to respond to PD-1 blockade, we analyzed the AUC (receiver operating characteristic (ROC)) for PD-1^T lymphocytes, CXCL13, B cells, TLS number and TLS area. All five of these parameters were strongly associated with anti-PD-1 response capacity, reaching an AUC $\geq$ 0.84 (Fig. 6g), indicating a high potential to identify those human tumors where intratumoral immune activity is held back by the PD-1 checkpoint.

Discussion

In this study, we provide a comprehensive analysis of the early intratumoral immune response to PD-1 blockade in five different human cancer types, as well as the tumor properties that predict this response. Using a PDTF system as the approach to perturb tumor microenvironments, we observed that such immunological responses can already be detected within 24–48 h after anti-PD-1 treatment in distinct cancer types. Importantly, these data provide evidence that capacity for intratumoral immune reactivation correlates closely with clinical response.

Seemingly contradictory data have been generated with respect to the question whether PD-1 blockade mainly reinvigorates tumor-resident T cells[27,36] or acts via recruitment of new T cell clones to the tumor site, a phenomenon referred to as 'clonal replacement'[2,4]. While observations made in lymph node samples may be more difficult to interpret, the current data obtained in non-lymph node lesions (9 out of 13 PDTF-Rs) provide strong evidence that PD-1 blockade can reactivate preexisting intratumoral T cells in human cancer lesions. Of note, since such reactivation is accompanied by

increased production of T cell chemoattractants such as CXCL9, CXCL10, CCL5 and CXCL13, the current data are consistent with a model where this reactivation may be a driver of the clonal replacement that has been observed in patients at later time points. Further work is required to understand whether PD-1 blockade can induce a durable reactivation of the already tumor-resident T cells or whether their capacity for reinvigoration may be limited in time, for example, due to fixed epigenetic changes[37,38]. We also note that the effects of LCK inhibition provide evidence for a smoldering T cell response in tumors that can be increased by PD-1 blockade. Thus, PD-1 blockade does not appear to reactivate a dormant but rather boost an ongoing T cell response.

Notably, while in some tumors nonresponse could be explained by either lack of immune cells or exclusion of CD8$^+$ T cells, which is consistent with clinical data[7,16,17], we identified a third subgroup of immunologically nonresponsive tumors that is characterized by a brisk intratumoral CD8$^+$ T cell infiltrate but largely lacks the secretion of proinflammatory cytokines and chemokines. Importantly, as based both on T cell phenotype and on direct testing of tumor reactivity, the capacity of the tumor-resident T cell pool to recognize tumor antigens appears to distinguish PD-1-responsive tumors from the three nonresponsive TMEs we identified.

The phenotype of the T cells detected in immune desert tumors analyzed in this study forms an outlier, with the few T cells present being strongly skewed toward a late dysfunctional state and with a depletion of the predysfunctional T cells detected in responding tumors. While further data are required, it may be speculated that these T cells represent the remainder of a 'failed immune response' in tumors that were once inflamed but have subsequently turned cold. The use of technologies that allow profiling of tumor reactivity of the intratumoral TCR repertoire in an unbiased manner[39], should be helpful to settle this issue. In such analyses, it will be useful to focus not only on the immune deserts among the melanoma, renal and lung cancers that are mostly represented in this study, but also include other 'cold' tumor types such as, for instance, pancreatic cancer.

The strong correlation between ex vivo and clinical responses raises the question whether the PDTF platform could allow prospective assessment of individual patient responses to PD-1 blockade. This may either entail the direct clinical application of the platform itself in addition to established biomarkers, such as PD-L1[16] or tumor mutational burden[40], or by deriving biomarkers (patterns) that can be measured using other less complex assay systems. In our view, the latter approach, with the PDTF platform primarily being exploited to dissect reactivity patterns and link these to tumor baseline properties would be most attractive.

Finally, paralleling the recent data that link the presence of TLS with clinical response to anti-PD-1 therapy[41–43], the current data reveal a link between the presence of TLS and capacity of intratumoral T cells to be reactivated by PD-1 blockade. Importantly, in addition to B cells, the dysfunctional PD-1^T TILs that have also been shown to be enriched in tumor reactivity predominantly localize in TLS[15], suggesting that the presence of these immune cell aggregates may be reflective of a structured ongoing antitumor immune response. In future work, combination of the PDTF platform described in this article with spatial profiling technologies[44–46] should allow one to determine whether TLS should solely be seen as hallmarks of inflamed tumors or whether these sites form the actual hotbeds for immune reactivation after PD-1 blockade in human cancer tissue.

Online content

Any methods, additional references, Nature Research reporting summaries, source data, extended data, supplementary information, acknowledgements, peer review information; details of author contributions and competing interests; and statements of data and code availability are available at https://doi.org/10.1038/s41591-021-01398-3.

Received: 28 April 2020; Accepted: 17 May 2021;
Published online: 8 July 2021

References

1. Xin Yu, J. et al. Trends in clinical development for PD-1/PD-L1 inhibitors. *Nat. Rev. Drug Discov.* **19**, 163–164 (2020).
2. Yost, K. E. et al. Clonal replacement of tumor-specific T cells following PD-1 blockade. *Nat. Med.* **25**, 1251–1259 (2019).
3. Wu, T. D. et al. Peripheral T cell expansion predicts tumour infiltration and clinical response. *Nature* **579**, 274–278 (2020).
4. Zhang, J. et al. Compartmental analysis of T-cell clonal dynamics as a function of pathologic response to neoadjuvant PD-1 blockade in resectable non-small cell lung cancer. *Clin. Cancer Res.* **26**, 1327–1337 (2020).
5. Strauss, L. et al. Targeted deletion of PD-1 in myeloid cells induces antitumor immunity. *Sci. Immunol.* **5**, eaay1863 (2020).
6. Mayoux, M. et al. Dendritic cells dictate responses to PD-L1 blockade cancer immunotherapy. *Sci. Transl. Med.* **12**, eaav7431 (2020).
7. Tumeh, P. C. et al. PD-1 blockade induces responses by inhibiting adaptive immune resistance. *Nature* **515**, 568–571 (2014).
8. Amaria, R. N. et al. Neoadjuvant immune checkpoint blockade in high-risk resectable melanoma. *Nat. Med.* **24**, 1649–1654 (2018).
9. Huang, A. C. et al. A single dose of neoadjuvant PD-1 blockade predicts clinical outcomes in resectable melanoma. *Nat. Med.* **25**, 454–461 (2019).
10. Neal, J. T. et al. Organoid modeling of the tumor immune microenvironment. *Cell* **175**, 1972–1988.e16 (2018).
11. Jenkins, R. W. et al. Ex vivo profiling of PD-1 blockade using organotypic tumor spheroids. *Cancer Discov.* **8**, 196–215 (2018).
12. Blank, C. et al. PD-L1/B7H-1 inhibits the effector phase of tumor rejection by T cell receptor (TCR) transgenic CD8$^+$ T cells. *Cancer Res.* **64**, 1140–1145 (2004).
13. Gros, A. et al. PD-1 identifies the patient-specific CD8$^+$ tumor-reactive repertoire infiltrating human tumors. *J. Clin. Invest.* **124**, 2246–2259 (2014).
14. Gros, A. et al. Prospective identification of neoantigen-specific lymphocytes in the peripheral blood of melanoma patients. *Nat. Med.* **22**, 433–438 (2016).
15. Thommen, D. S. et al. A transcriptionally and functionally distinct PD-1$^+$ CD8$^+$ T cell pool with predictive potential in non-small-cell lung cancer treated with PD-1 blockade. *Nat. Med.* **24**, 994–1004 (2018).
16. Herbst, R. S. et al. Predictive correlates of response to the anti-PD-L1 antibody MPDL3280A in cancer patients. *Nature* **515**, 563–567 (2014).
17. Sharma, P. & Allison, J. P. The future of immune checkpoint therapy. *Science* **348**, 56–61 (2015).
18. Hegde, P. S., Karanikas, V. & Evers, S. The where, the when, and the how of immune monitoring for cancer immunotherapies in the era of checkpoint inhibition. *Clin. Cancer Res.* **22**, 1865–1874 (2016).
19. Galon, J. & Bruni, D. Approaches to treat immune hot, altered and cold tumours with combination immunotherapies. *Nat. Rev. Drug Discov.* **18**, 197–218 (2019).
20. Sanmamed, M. F. et al. Changes in serum interleukin-8 (IL-8) levels reflect and predict response to anti-PD-1 treatment in melanoma and non-small-cell lung cancer patients. *Ann. Oncol.* **28**, 1988–1995 (2017).
21. Schalper, K. A. et al. Elevated serum interleukin-8 is associated with enhanced intratumor neutrophils and reduced clinical benefit of immune-checkpoint inhibitors. *Nat. Med.* **26**, 688–692 (2020).
22. Yuen, K. C. et al. High systemic and tumor-associated IL-8 correlates with reduced clinical benefit of PD-L1 blockade. *Nat. Med.* **26**, 693–698 (2020).
23. Wherry, E. J. et al. Molecular signature of CD8$^+$ T cell exhaustion during chronic viral infection. *Immunity* **27**, 670–684 (2007).
24. Baitsch, L. et al. Extended co-expression of inhibitory receptors by human CD8 T-cells depending on differentiation, antigen-specificity and anatomical localization. *PLoS ONE* **7**, e30852 (2012).
25. Thommen, D. S. et al. Progression of lung cancer is associated with increased dysfunction of T cells defined by coexpression of multiple inhibitory receptors. *Cancer Immunol. Res.* **3**, 1344–1355 (2015).
26. Kurtulus, S. et al. Checkpoint blockade immunotherapy induces dynamic changes in PD-1$^-$CD8$^+$ tumor-infiltrating T cells. *Immunity* **50**, 181–194.e6 (2019).
27. Siddiqui, I. et al. Intratumoral Tcf1$^+$PD-1$^+$CD8$^+$ T cells with stem-like properties promote tumor control in response to vaccination and checkpoint blockade immunotherapy. *Immunity* **50**, 195–211.e10 (2019).
28. Miller, B. C. et al. Subsets of exhausted CD8$^+$ T cells differentially mediate tumor control and respond to checkpoint blockade. *Nat. Immunol.* **20**, 326–336 (2019).
29. Sade-Feldman, M. et al. Defining T cell states associated with response to checkpoint immunotherapy in melanoma. *Cell* **175**, 998–1013.e20 (2018).

30. Krishna, S. et al. Stem-like CD8 T cells mediate response of adoptive cell immunotherapy against human cancer. *Science* **370**, 1328–1334 (2020).
31. Duhen, T. et al. Co-expression of CD39 and CD103 identifies tumor-reactive CD8 T cells in human solid tumors. *Nat. Commun.* **9**, 2724 (2018).
32. Byrne, A. et al. Tissue-resident memory T cells in breast cancer control and immunotherapy responses. *Nat. Rev. Clin. Oncol.* **17**, 341–348 (2020).
33. Edwards, J. et al. CD103$^+$ tumor-resident CD8$^+$ T cells are associated with improved survival in immunotherapy-naïve melanoma patients and expand significantly during anti-PD-1 treatment. *Clin. Cancer Res.* **24**, 3036–3045 (2018).
34. Menares, E. et al. Tissue-resident memory CD8$^+$ T cells amplify anti-tumor immunity by triggering antigen spreading through dendritic cells. *Nat. Commun.* **10**, 4401 (2019).
35. Ansel, K. M. et al. A chemokine-driven positive feedback loop organizes lymphoid follicles. *Nature* **406**, 309–314 (2000).
36. Gettinger, S. N. et al. A dormant TIL phenotype defines non-small cell lung carcinomas sensitive to immune checkpoint blockers. *Nat. Commun.* **9**, 3196 (2018).
37. Schietinger, A. et al. Tumor-specific T cell dysfunction is a dynamic antigen-driven differentiation program initiated early during tumorigenesis. *Immunity* **45**, 389–401 (2016).
38. Philip, M. et al. Chromatin states define tumour-specific T cell dysfunction and reprogramming. *Nature* **545**, 452–456 (2017).
39. Scheper, W. et al. Low and variable tumor reactivity of the intratumoral TCR repertoire in human cancers. *Nat. Med.* **25**, 89–94 (2019).
40. Rizvi, N. A. et al. Cancer immunology. Mutational landscape determines sensitivity to PD-1 blockade in non-small cell lung cancer. *Science* **348**, 124–128 (2015).
41. Helmink, B. A. et al. B cells and tertiary lymphoid structures promote immunotherapy response. *Nature* **577**, 549–555 (2020).
42. Petitprez, F. et al. B cells are associated with survival and immunotherapy response in sarcoma. *Nature* **577**, 556–560 (2020).
43. Cabrita, R. et al. Tertiary lymphoid structures improve immunotherapy and survival in melanoma. *Nature* **577**, 561–565 (2020).
44. Decalf, J., Albert, M. L. & Ziai, J. New tools for pathology: a user's review of a highly multiplexed method for in situ analysis of protein and RNA expression in tissue. *J. Pathol.* **247**, 650–661 (2019).
45. Rodriques, S. G. et al. Slide-seq: a scalable technology for measuring genome-wide expression at high spatial resolution. *Science* **363**, 1463–1467 (2019).
46. Vickovic, S. et al. High-definition spatial transcriptomics for in situ tissue profiling. *Nat. Methods* **16**, 987–990 (2019).

Methods

Patient characteristics and tumor sample processing. Tumor samples were collected from individuals with melanoma, NSCLC, breast cancer, ovarian cancer or renal cell carcinoma undergoing surgical treatment between April 2017 and January 2020 at the Netherlands Cancer Institute-Antoni van Leeuwenhoekziekenhuis (NKI-AVL). Detailed patient characteristics are provided in Supplementary Tables 1–3. The study was approved by the institutional review board of the NKI-AVL and performed in compliance with all relevant ethical regulations. All patients consented to research usage of material not required for diagnostic use either by opt-out procedure or via previous written informed consent (after 23 May 2018).

Solid tumor lesions were macroscopically selected by a pathologist from the resected tumor material and part of the tumor was collected in ice-cold collection medium (Roswell Park Memorial Institute (RPMI) 1640 medium (Thermo Fisher Scientific) supplemented with 2.5% FBS (Sigma-Aldrich), 1% penicillin-streptomycin (Roche)) for subsequent PDTF cultures. A second part of the tumor was embedded in paraffin for histological analysis and for analysis of tumor cell content within the collected lesion. Tissue materials collected for subsequent PDTF cultures were immediately processed by manual cutting into small tumor fragments (PDTFs) of 1–2 mm^3 size on ice. After processing, a number of single PDTFs from different regions within a tumor were mixed to ensure uniform representation of the tumor lesion (Extended Data Fig. 1a) and were frozen in cryovials containing 1 ml of FBS with 10% dimethylsulfoxide (Sigma-Aldrich) with 8–15 PDTFs per vial. All PDTFs were cryopreserved in liquid nitrogen until further usage.

PDTF cultures. To prevent lymphocyte efflux, individual PDTFs were embedded in artificial extracellular matrix prepared as follows: first, sodium bicarbonate (1.1% final concentration (Sigma-Aldrich)), collagen I (1 mg ml^{-1} final concentration; Corning) and tumor medium (DMEM (Thermo Fisher Scientific) supplemented with 1 mM of sodium pyruvate (Sigma-Aldrich), 1× MEM nonessential amino acids (Sigma-Aldrich), 2 mM of L-glutamine (Thermo Fisher Scientific), 10% FBS and 1% penicillin-streptomycin were slowly mixed. All components were kept ice-cold to avoid premature solidification of the collagen. Next, ice-cold Matrigel (Matrix High Concentration, Phenol Red-Free, 4 mg ml^{-1} final concentration; BD Biosciences) was added to the mix very slowly. To prepare a tumor matrix that only contained collagen, the last step was omitted. For matrices with distinct glucose concentration, the standard DMEM medium (4,500 mg l^{-1} D-glucose) was replaced with either low-glucose DMEM (1,000 mg l^{-1} D-glucose; Thermo Fisher Scientific) or RPMI 1640 (2,000 mg l^{-1} D-glucose). To assess the effect of the type or concentration of serum, either 2% or 20% FBS or 10% human serum (Sigma-Aldrich) were used instead of 10% FBS. Each well of a precooled 96-well plate was coated with 40 µl of matrix to serve as a bottom layer and matrix was solidified by exposure to 37 °C for 20–30 min.

Vials with cryopreserved PDTFs were thawed in a water bath at 37 °C until only a small drop of ice remained. PDTFs were then transferred into a 50-ml tube and slowly thawed by dropwise addition of 10 ml of prewarmed tumor medium. Next, PDTFs were extensively washed in tumor medium by flushing them multiple times on a cell strainer in a 6-well plate. One PDTF per well was placed on top of the presolidified matrix, after which a second layer of 40-µl matrix was added. Plates were then placed in a 37 °C incubator for 20–30 min. After solidification, 120 µl of tumor medium was added on top of the matrix. Where indicated, tumor medium was supplemented with either anti-PD-1 antibody (nivolumab; Bristol Myers Squibb) at 10 µg ml^{-1} final concentration or anti-CD3 (OKT3; BioLegend) at 5 µg ml^{-1} final concentration either alone or in combination with anti-CD28 (CD28.2; BioLegend) at 2 µg ml^{-1} final concentration. Control cultures were carried out in the presence of control human anti-β-Gal-hIgG4 (S228P; InvivoGen) at 10 µg ml^{-1}. Eight to ten PDTFs were used per condition. Unless indicated otherwise, PDTF cultures were kept at 37 °C for 48 h before readout.

Flow cytometry analysis of PDTFs. PDTFs were analyzed by flow cytometry to assess T cell activation after culture and determine immune cell composition and T cell state at baseline using the following antibodies. T cell activation analysis: anti-CD45 PerCP Cy5.5 (clone 2D1, 1:100 dilution), anti-CD3 APC-eFluor 780 (clone SK7; 1:50 dilution) and anti-ICOS FITC (clone ISA-3; 1:25 dilution), all from Invitrogen; anti-CD3 FITC (clone SK7; 1:50 dilution), anti-CD8 BV605 (clone RPA-T8; 1:100 dilution), anti-CD4 BV421 (clone SK3; 1:100 dilution), anti-OX40 APC (clone BerACT35; 1:20 dilution) and anti-CD25 AF700 (clone BC96; 1:20 dilution), all from BioLegend; anti-PD-1 PE-Cy7 (clone EH12.1; 1:20 dilution), anti-CD137 PE (clone 4B4-1; 1:20 dilution) and anti-CD137 BUV395 (clone 4B4-1; 1:50 dilution), all from BD Biosciences; anti-IFNγR1 PE (clone 92101; 1:25 dilution), from R&D systems. Immune composition and T cell state analysis: anti-CD45 PerCP Cy5.5 (1:100 dilution), anti-CTLA-4 FITC (clone 14D3; 1:50 dilution), anti-TIGIT PE (clone MBSA43; 1:20 dilution) and anti-LAG3 APC (clone 3DS223H; 1:20 dilution), all from Invitrogen; anti-CD8 BUV563 (clone RPA-T8; 1:50 dilution), anti-CD3 BV711 (clone UCHT1; 1:50 dilution), anti-PD-1 PE-Cy7 (clone EH12.1; 1:20 dilution) and anti-CD103 BV421 (clone Ber-ACT8; 1:20 dilution), all from BD Biosciences; anti-CD3 FITC (1:50 dilution), anti-CD4 BV421 (clone SK3; 1:100 dilution), anti-CD19 BV605 (clone SJ25C1; 1:50 dilution), anti-FOXP3 AF647 (clone 259D; 1:50 dilution), anti-CD11c PE (clone Bu15; 1:50 dilution), anti-CD16 Alexa 700 (clone 3G8; 1:50 dilution), anti-TIM-3 BV421 (clone F38-2E2; 1:20 dilution), anti-CD39 FITC (clone A1; 1:20 dilution) and anti-TCF1 PE (clone 7F11A10; 1:20 dilution), all from BioLegend. Myeloid cell, fibroblast and endothelial cell analysis: anti-CD45 PerCP-Cy5.5 (1:100 dilution) from Invitrogen; anti-lineage cocktail CD3/CD19/CD20/CD56 APC (clones UCHT1, HIB19, 2H7, 5.1H11; 1:50 dilution), anti-CD11b BV605 (clone ICRF44; 1:50 dilution), anti-CD68 FITC (clone Y1/82A; 1:50 dilution), anti-CD206 PE-Cy7 (clone 15-2; 1:20 dilution), anti-CD14 AF700 (clone M5E2; 1:200 dilution), anti-CD123 BV421 (clone 6H6; 1:100 dilution), anti-PD-L1 (clone 29E.2A3; 1:100 dilution), all from BioLegend; anti-CD11c PE-CF594 (clone 3.9; 1:200 dilution), anti-HLA-DR BUV395 (clone L243af; 1:100 dilution), anti-CD31 BV480 (clone WM-59; 1:100 dilution), anti-CD86 BUV563 (clone FUN-1; 1:50 dilution), all from BD Biosciences; anti-FAPα PE (clone 427819; 1:20 dilution) from R&D systems.

For analysis of PD-1 blockade effects, PDTFs were manually retrieved from the matrix after 48 h of culture, pooled for each experimental condition and processed into single-cell suspensions by enzymatic digestion in digestion mix (RPMI 1640 medium supplemented with 1% penicillin-streptomycin, 12.6 µg ml^{-1} Pulmozyme (Roche) and 1 mg ml^{-1} collagenase type IV (Sigma-Aldrich)) for 1 h at 37 °C and under slow rotation. Samples were then washed in PBS (Sigma-Aldrich), filtered over a 150-µM filter mesh, resuspended in 50 µl of PBS and incubated with Fc receptor blocking agent (eBioscience) and with either LIVE/DEAD IR Dye (Thermo Fisher Scientific) or Zombie UV (BioLegend) for 20 min at 4 °C. Cells were washed, resuspended in 50 µl of staining buffer (PBS, 0.5% bovine serum albumin (Sigma-Aldrich) and 0.1% NaN_3 (Invitrogen)) containing the aforementioned antibodies and incubated for 20 min at 4 °C. After washing twice, cells were taken up in 200 µl of IC Fixation Buffer (eBioscience) and incubated for 20 min. Subsequently, samples were washed twice before data acquisition.

For the analysis of immune infiltrates and T cell states, PDTFs were thawed and immediately digested as described above. Samples were resuspended in 50 µl of PBS and incubated with Fc receptor blocking agent and with either LIVE/DEAD IR Dye or Zombie UV for 20 min at 4 °C. Cells were then washed, resuspended in 50 µl of staining buffer containing the aforementioned antibodies and incubated for 20 min at 4 °C. For intracellular staining, cells were washed twice, fixed and permeabilized using Fix & Perm solution (eBioscience) for 30 min at room temperature. After washing twice, cells were resuspended in 1× permeabilization buffer (eBioscience) containing antibodies for 40 min at room temperature. Subsequently, samples were washed twice before data acquisition.

Data acquisition was carried out on a BD LSR II SORP, a Fortessa SORP or a Symphony A5 SORP cell analyzer (all from BD Biosciences). Data were collected using the BD FACSDiva Software v.8.0.1 (LSR II SORP), v.8.0.2 (Fortessa SORP) and v.8.5 (Symphony A5 SORP) and further analyzed with FlowJo v.10.6.1 (FlowJo LLC) and Prism v.8.0e (GraphPad Software). Analysis of coexpression of inhibitory receptors was performed using SPICE v.6.0045[47]. Clustering analyses were performed using the FlowJo plugins UMAP[48] and X-Shift[49]. An example of the gating strategy is shown in Supplementary Fig. 4.

IHC and digital image analyses. IHC of sectioned tumor samples was performed on a BenchMark ULTRA Instrument (Roche Diagnostics). In brief, serial 3-µm sections were cut from formalin-fixed, paraffin-embedded tumor samples. Sections were heated at 75 °C for 28 min and deparaffinized in the Instrument with EZ Prep solution (Ventana Medical Systems). Heat-induced epitope retrieval was carried out using Cell Conditioning 1 (Ventana Medical Systems) for 32 min at 95 °C (CD4, CD8, CD3 and CD20) or for 48 min at 95 °C (PD-1). Sections were then stained with monoclonal antibodies against CD4 (clone SP35; 1:25 dilution; Cell Marque), CD8 (clone C8/144B; 1:200 dilution; DAKO/Agilent), CD20 (clone L26; 1:800 dilution, DAKO/Agilent), CD3 (clone SP7; 1:100 dilution; Spring/ITK) for 32 min at 37 °C and PD-1 (clone NAT105; ready-to-use; Roche) for 16 min at room temperature. Antibodies were detected using 3,3′-diaminobenzidine (DAB) (OptiView Detection Kit; Ventana Medical Systems). Slides were counterstained with Hematoxylin and Bluing Reagent (Ventana Medical Systems).

Slides were scanned at ×20 magnification using an Aperio AT2 slide scanner (Leica Biosystems) and data were uploaded on Slide Score (www.slidescore.com). Tumor lesions were digitally annotated using the HALO image analysis software v.2.3 (Indica Labs). To quantify $CD8^+$ cells at single-cell resolution, we developed a digital image approach based on the HALO multiplex IHC v.1.2 base algorithm. Color deconvolution was performed both for the nuclear counterstain (RGB 0.179, 0.164, 0.106) and the DAB product (RGB 0.324, 0.482, 0.628). For regional analysis, classifiers were trained to identify stromal and tumor regions (the latter defined as regions containing cancer cells), where $CD8^+$ T cells were quantified separately. Excluded tumors were defined as all immune-rich tumors (≥10% $CD45^+$ cells in the flow cytometry analysis) with both a low tumoral $CD8^+$ T cell count, corresponding to 0 or +1 scoring by an experienced pathologist (average $CD8^+$ T cell count excluded tumors: 45.5 (range 1.96–160.9) $CD8^+$ mm^{-2}, average $CD8^+$ T cell count infiltrated tumors: 564.3 (53.5–1764.7) $CD8^+$ mm^{-2}) and a fivefold higher or more $CD8^+$ T cell count in the stromal region than in the tumor region (excluded: 526.6 (95.1–1087.9); infiltrated: 1165.2 (106.3–3046.4) $CD8^+$ mm^{-2}).

For quantification of TLS, TLS were manually identified and quantified (TLS mm^{-2}) as based on the presence of B cell (CD20) and T cell (CD3, CD4 and

CD8) zones. TLS areas were measured using digital annotation and quantification by HALO. Lymphoid aggregates < 60,000 μm² were excluded as described previously[20]. Average TLS areas were obtained by dividing the total TLS area by the number of TLS present.

Analysis of secreted mediators. For the analysis of cytokines, chemokines and cytotoxic mediators, the supernatants of PDTF cultures were collected after 48 h of culture, unless indicated otherwise. Supernatants were immediately frozen and preserved at −80 °C. Supernatants were thawed on ice and the supernatants from each condition were pooled, except for single-fragment analyses, and the presence of the indicated cytokines and chemokines was detected using the LEGENDplex Human Th Cytokine, Human Proinflammatory Chemokine, customized Human Proinflammatory Chemokine and Human CD8/NK panels (all from BioLegend) or using the BLC/CXCL13 Human ELISA Kit (Thermo Fisher Scientific) according to the manufacturers' instructions.

Antibody penetration. To measure the penetration of antibodies added exogenously into tumor fragments, fluorescently labeled antibodies recognizing different surface antigens (anti-CD8 AF594 nanobody (clone 218; 1:100 dilution[50]) and anti-EpCAM AF647 (clone 9C4; 1:50 dilution: BioLegend)) were added to PDTF cultures for the indicated time periods. For subsequent analysis by flow cytometry, PDTFs were processed into single-cell suspensions as described above and samples were counterstained using an anti-CD8 PE antibody (clone B9.11; 1:100 dilution; Beckman Coulter) that binds a nonoverlapping epitope. Overlap in signal for the two antibodies was then determined by flow cytometry. For subsequent analysis by immunofluorescence, PDTFs were washed, fixed in 4% paraformaldehyde for 2 h and snap-frozen in optimal cutting temperature compound (CellPath). Sectioning was performed on a microtome-cryostat (CM1950; Leica Biosystems). Tissue sections were stained with an anti-EpCAM PE antibody (clone EBA-1; 1:50 dilution; BD Biosciences) that binds a nonoverlapping epitope and 4,6-diamidino-2-phenylindole (DAPI) for nuclear counterstaining. Images were acquired on a BX63 Apollo fluorescence microscope (Olympus) and analyzed using ImageJ v.1.47.

Sorting and in vitro expansion of intratumoral T cells. To isolate intratumoral T lymphocytes, cryopreserved PDTFs were thawed and digested as described above. Samples were resuspended in 300 μl of staining buffer containing the following antibodies: anti-CD45 PerCP Cy5.5 (1:100 dilution) from Invitrogen; anti-CD3 PE (clone SK7; 1:50 dilution), anti-CD19 APC (clone SJ25C1; 1:50 dilution), anti-CD56 APC (clone HCD56; 1:20 dilution), anti-CD16 APC (clone 3G8; 1:50 dilution), anti-CD11b APC (clone ICRF44; 1:50 dilution) and anti-CD11c APC (clone 3.9; 1:50 dilution) from BioLegend. After 20 min incubation at 4 °C, cells were washed twice and cell sorting was performed on a BD FACSAria Fusion SORP cell sorter (v.8.0.1; BD Biosciences). Cells were sorted on side scatter-area/forward scatter-area, forward scatter-area/forward scatter-height for singlets and live cells (DAPI-negative; Sigma-Aldrich) and T cells, identified as $CD45^+$, bulk $CD19^-$, $CD56^-$, $CD16^-$, $CD11b^-$, $CD11c^-$ and $CD3^+$ cells. Postsort sample purity was >98%. Sorted cells were rested at 37 °C in T cell medium (50% CTS AIM V medium (Thermo Fisher Scientific), 50% RPMI 1640 medium, no phenol red (Thermo Fisher Scientific), 10% human serum, 1% penicillin-streptomycin and 2 mM of L-glutamine). After 2 h, cells were expanded in vitro using an excess of irradiated allogeneic feeder cells (4,000 rad) pooled from 3 healthy donors in T cell medium supplemented with 3,000 IU ml^{-1} of IL-2 (PeproTech) and 30 ng ml^{-1} anti-CD3 (OKT3)[13,15]. From day 7 onward, half of the medium was replaced with fresh medium containing IL-2 every 2–3 d. Cells were split 1:2 on day 7 and when necessary. From day 15, T cells were further cultured in T cell medium containing 60 IU ml^{-1} of IL-2 (PreproTech) and cells were cryopreserved on day 18.

Assessment of tumor reactivity. The cryopreserved intratumoral T lymphocytes that were expanded in vitro were thawed and cultured in T cell medium containing 60 IU ml^{-1} of IL-2 for 3 d. Subsequently, cells were washed in PBS and fluorescently labeled with 5 μM of CellTrace Violet (Thermo Fisher Scientific). Autologous PDTFs were thawed and digested as described above and cells were rested for 1 h at 37 °C in complete medium (RPMI 1640 medium, 10% human serum, 1% penicillin-streptomycin, 1 mM of sodium pyruvate (Sigma-Aldrich) and 1× MEM nonessential amino acids).

CellTrace Violet-labeled T cells ($1–2 \times 10^5$) were cocultured with autologous digest at an effector:tumor cell ratio of 1:1. The percentage of tumor cells in the digests was estimated previously by flow cytometry gating on $CD45^-$, forward scatter-high cells. A condition with a blocking antihuman leukocyte antigen (HLA) class I antibody (hybridoma W6/32 purified in house, 10 μg ml^{-1}) was included to determine HLA class I restriction of any observed T cell responses. T cells cultured in the absence of tumor digest, with or without 10 ng ml^{-1} of phorbol 12-myristate 13-acetate (Sigma-Aldrich) and 200 ng ml^{-1} of ionomycin (Sigma-Aldrich) were used as further controls. After 1 h of culture, 1× monensin (BD Biosciences) and 1× brefeldin A (BD Biosciences) were added and cells were incubated for an additional 16 h before analysis of IFN-γ (anti-IFN-γ APC; clone 4S.B3; 1:50 dilution; BioLegend) and TNF-α (anti-TNFα PE-Cy7; clone MAb11; 1:50 dilution; BD Biosciences) production by intracellular cytokine staining and flow cytometry. HLA class I expression was detected using anti-HLA ABC FITC (clone W6/32; 1:50 dilution; BioLegend) antibody.

Modulation of anti-PD-1 response. To establish optimal conditions for IFNγR1 and LCK blockade, healthy donor PBMCs (Sanquin) were cultured in tumor medium in the absence or presence of either LCK inhibitor (LCKi, CAS no. 213743-31-8; Merck Millipore) or anti-IFN-γ R1 blocking antibody (aIFNγR1; catalog no. 92101, R&D Systems). After 1 (aIFNγR1) or 2 h (LCKi) of culture, PBMCs were transferred to a plate coated with anti-CD3 (OKT3, 5 μg ml^{-1})/anti-CD28 (clone 28.2, 2 μg ml^{-1}) antibodies and cells were cultured in the continued presence of LCKi or aIFNγR1 for 48 h. Subsequently, T cell activation and CXCL10 production were assessed by flow cytometry using the Human IP-10 Flex Set kit (BD Biosciences).

In PDTF cultures, either 8 μM of LCKi or 50 μg ml^{-1} of aIFNγR1 antibody was added for 2 and 1 h, respectively before ex vivo anti-PD-1 treatment. Samples that were cultured in the absence or presence of anti-PD-1 alone were taken along as control. Cultures were incubated at 37 °C and analyzed after 48 h.

Statistical analysis. Data are reported as the mean ± s.d. or the mean ± s.e.m., as specified. Statistical significance was determined using the Mann–Whitney *U*-test, two-tailed Wilcoxon test or Kruskal–Wallis test, as indicated (Prism v.8.0e). Differences were considered statistically significant if $^*P < 0.05$, $^{**}P < 0.01$, $^{***}P < 0.001$, $^{****}P < 0.0001$. Only significant *P* values are displayed. Correlations were evaluated using Spearman rank-order correlation and effect sizes were calculated using Hedge's *g*. All computational analyses were performed in R v.4.0.2. Unless otherwise specified, experiments were performed without duplicates because of material restrictions. Data describing reproducibility of cultures are provided in Fig. 2f, Extended Data Figs. 1d,e and 3a–d and Supplementary Fig. 1.

The PDTF response score was developed by first calculating the ROC curves based on the delta values (anti-PD-1-treated condition minus untreated condition) for each parameter measured in the original cohort. Twelve parameters that were strongly discriminative between responders and nonresponders were selected based on the AUC-ROC curve (Extended Data Fig. 4a,b). For each parameter, a cutoff value was identified aiming for high specificity and sensitivity. This cutoff was used to score each parameter in each sample depending on whether the delta value was above or below the cutoff. Parameters with a specificity >90% were weighted double (Extended Data Fig. 4c). The response score was calculated as follows:

$$\text{PDTF response score} = \frac{\sum \text{all parameters}}{\text{maximal score}} \times 100$$

Reporting Summary. Further information on research design is available in the Nature Research Reporting Summary linked to this article.

Data availability

All relevant flow cytometry, immunohistochemistry and cytokine/chemokine data are provided as supplementary data.

Code availability

No custom code was developed. All code used in this study is either specified in the Methods or available from the corresponding author.

References

47. Roederer, M., Nozzi, J. L. & Nason, M. C. SPICE: exploration and analysis of post-cytometric complex multivariate datasets. *Cytometry A* **79**, 167–174 (2011).
48. McInnes, L., Healy, J. & Melville, J. UMAP: uniform manifold approximation and projection for dimension reduction. Preprint at *arXiv* https://arxiv.org/abs/1802.03426v3 (2020).
49. Samusik, N., Good, Z., Spitzer, M. H., Davis, K. L. & Nolan, G. P. Automated mapping of phenotype space with single-cell data. *Nat. Methods* **13**, 493–496 (2016).
50. Dijkgraaf, F. E. et al. Tissue patrol by resident memory $CD8^+$ T cells in human skin. *Nat. Immunol.* **20**, 756–764 (2019).

Acknowledgements

We thank D. Peters and the NKI-AVL Core Facility for Molecular Pathology & Biobanking for supplying and processing the NKI-AVL Biobank material, the NKI-AVL flow cytometry facility for assistance with sorting and flow cytometric analyses, L. Rozeman for assistance with the acquisition of clinical data and all members of the Thommen and Schumacher laboratories for helpful discussions. This work was supported by a PhD fellowship from the Portuguese Foundation for Science and Technology (no. SFRH/BD/52042/2012) through the Graduate Program in Basic and Applied Biology to P.V., by a KWF Young investigator grant (no. 12046) and the Swiss National Science Foundation (no. P300PB_177881) to D.S.T. and by an ERC AdG SENSIT grant (no. 742259) to T.N.S.

Author contributions

T.N.S. and D.S.T. conceived the study. P.V., L.M.R., A.Z., J.B.A.G.H., T.N.S. and D.S.T. conceived the experimental design. P.V., M.d.B., L.M.R., S.H.H., S.B., M.v.d.B. and P.H. performed the experiments. P.V., M.d.B., L.M.R., T.N.S. and D.S.T. analyzed the data. A.B., C.U.B., K.J.H. and K.M. contributed to the collection of patient samples and data. J.S. and K.M. performed the pathological characterization of patient samples. L.M.R., J.S. and K.M. performed the digital image analysis. P.V., T.N.S. and D.S.T. wrote the manuscript. All authors reviewed and edited the manuscript.

Competing interests

T.N.S. is an advisor to Adaptive Biotechnologies, Allogene Therapeutics, Merus, Neogene Therapeutics and Scenic Biotech. He is a recipient of research support from Merck KGaA, a stockholder in Allogene Therapeutics, Merus, Neogene Therapeutics and Scenic Biotech and is venture partner at Third Rock Ventures, all outside of the current work. D.S.T. received research funding from Bristol Myers Squibb, outside of the current work. The other authors declare no competing interests.

Additional information

Extended data is available for this paper at https://doi.org/10.1038/s41591-021-01398-3.

Supplementary information The online version contains supplementary material available at https://doi.org/10.1038/s41591-021-01398-3.

Correspondence and requests for materials should be addressed to D.S.T.

Peer review information *Nature Medicine* thanks Karuna Ganesh and the other, anonymous, reviewer(s) for their contribution to the peer review of this work. Javier Carmona was the primary editor on this article and managed its editorial process and peer review in collaboration with the rest of the editorial team.

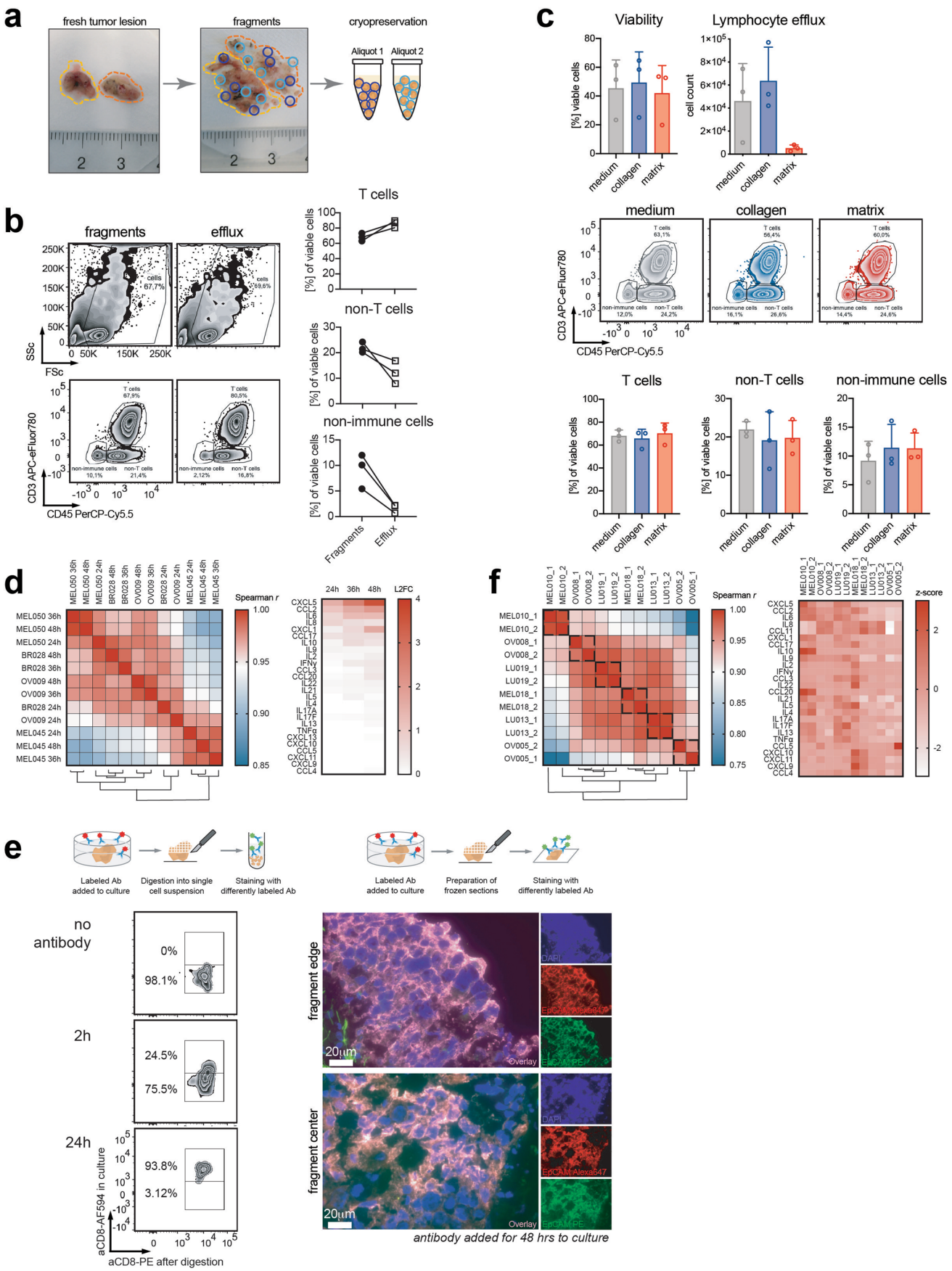

Extended Data Fig. 1 | See next page for caption.

Extended Data Fig. 1 | Development and validation of ex vivo patient-derived tumor fragment (PDTF) cultures. a, Macroscopic image of a lung tumor processed into PDTFs. PDTFs from distinct tumor regions were mixed to offset the effects of tumor heterogeneity and were immediately cryopreserved. **b**, Flow plots showing total live cells and T cell ($CD45^+CD3^+$), non-T cell ($CD45^+CD3^-$) and non-immune cell subsets ($CD45^-CD3^-$) of digested PDTFs and culture supernatant after 48 h of culture in absence of the matrix (left), and quantification of these subsets in three tumor samples (right). **c**, Viability and lymphocyte efflux (measured by manual counting of cells in culture supernatants) of PDTFs cultured for 48 h in either medium, collagen, or complete matrix (top), and quantification of T cells ($CD45^+CD3^+$), non-T cells ($CD45^+CD3^-$) and non-immune cells ($CD45^-CD3^-$) in PDTFs cultured in these conditions. Representative flow plots (middle) and mean and s.e.m. of three PDTF cultures (bottom) are depicted. **d**, Correlation matrix depicting the Spearman co-efficient (left) and heatmap (right) of cytokine/chemokine measurements performed at 24, 36, and 48 h of PDTF cultures for four different tumors. The $\log_2$ fold change (L2FC) relative to the matching 12 h sample is depicted. **e**, Antibody penetration assays, comparing overlap in fluorescence of two antibodies recognizing different epitopes of the same target. Antibodies were either added to the culture at indicated time points, or were used for subsequent staining after tissue processing into single cell suspensions (anti-CD8, left), or tissue slides (anti-EpCAM, right). Shown is one of 4 independent experiments. **f**, Correlation matrix depicting the Spearman co-efficient (left) and heatmap (right) of cytokine/chemokine measurements at 48 h in two parallel cultures from each tumor for six different tumors. Normalized values for each parameter are depicted.

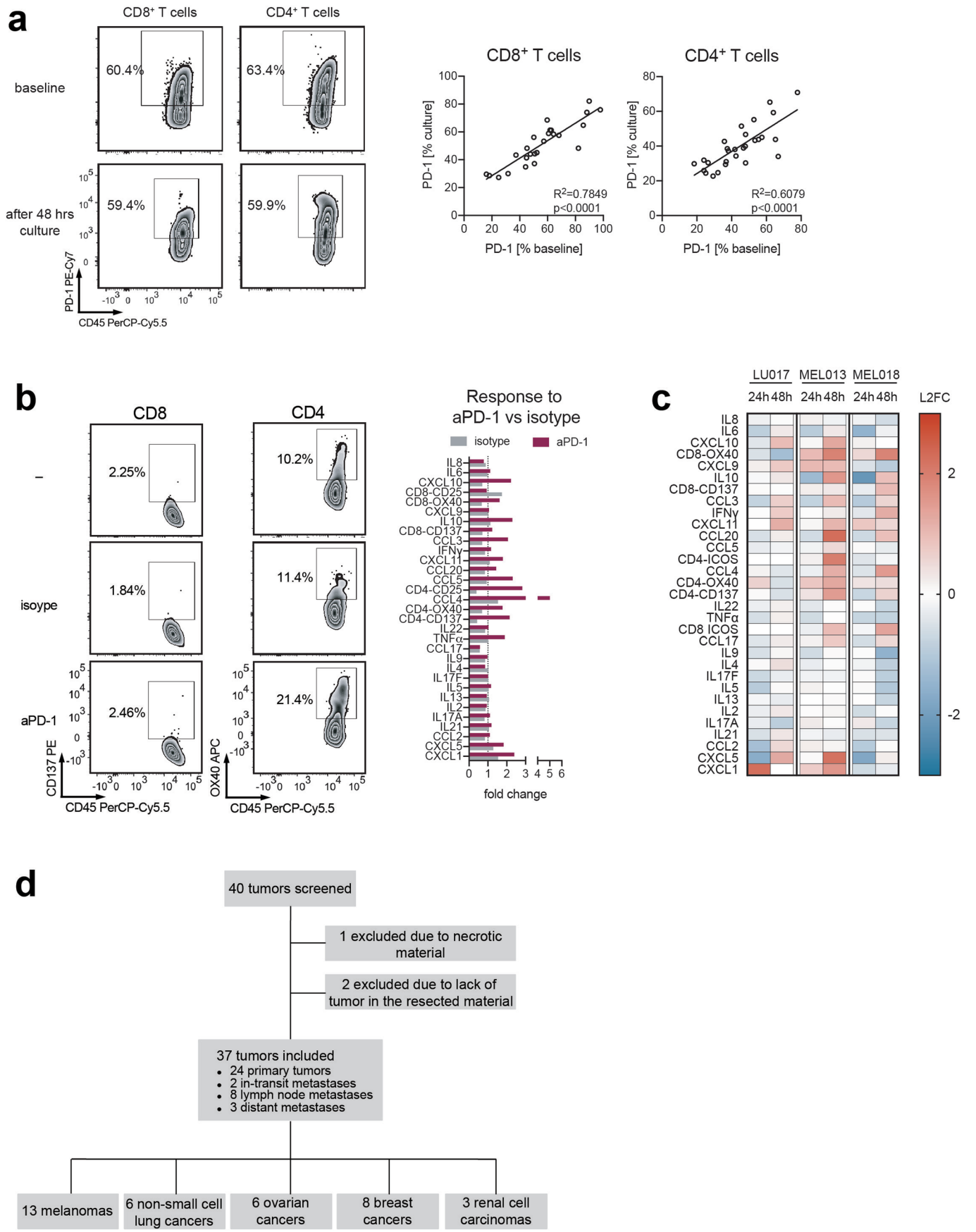

Extended Data Fig. 2 | See next page for caption.

Extended Data Fig. 2 | Ex vivo treatment of PDTFs with anti-PD-1. a, Representative flow plot (LU019) and correlation of PD-1 expression analyzed directly ex vivo and after 48 h of culture on either $CD8^+$ (left) or $CD4^+$ (right) T cells (n = 37). **b**, T cell activation (LU019) and cytokine/chemokine secretion upon either anti-PD-1 or a matching human IgG4 (S228P) isotype control treatment. The bar graph indicates the fold change compared to the untreated culture. **c**, Comparison of ex vivo anti-PD-1 treatment for 24 h and 48 h, expressed as $\log_2$ fold change (L2FC) relative to untreated PDTFs (n = 3). **d**, Study cohort overview.

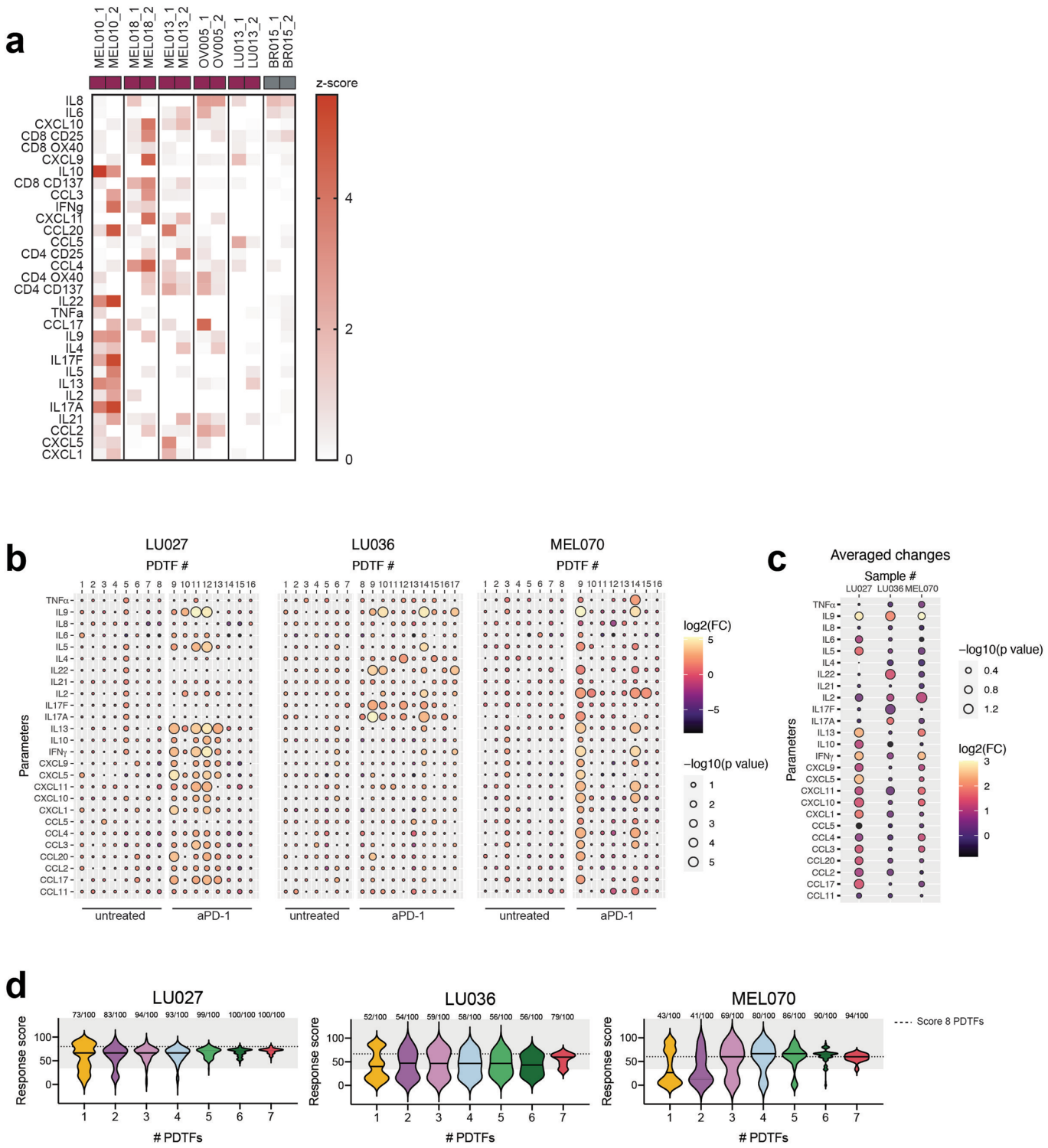

Extended Data Fig. 3 | Reproducibility of PDTF responses. a, T cell activation and cytokine/chemokine profiling upon PD-1 blockade in two independently performed PDTF cultures for five responding tumors and one non-responding tumor. Normalized delta values between the treated and the untreated condition are depicted. **b**, Immunological responses of individual tumor fragments. The fold change and *P* value for each parameter of each untreated or anti-PD-1 treated fragment was calculated against the mean of all untreated fragments (n = 3 PDTF-R tumors). **c**, Fold change and *P* value for each parameter of averaged anti-PD-1 treated versus untreated PDTFs from the same experiment as in (**b**). Significance in **b** and **c** were calculated for each parameter and comparison by unpaired two-sample t test with two-stage linear step-up procedure of Benjamini, Krieger and Yekutieli. **d**, Violin plots showing the range of response scores (as defined in Extended Data Fig. 4) for 100 randomly selected combinations of 1-7 individual tumor fragments for both the untreated and anti-PD-1 treated condition. Data are derived from the experiment shown in (**b**). The dashed line indicates the response score when using data from all 8 tumor fragments, as done in standard PDTF cultures, the grey shaded area indicates a positive response score. Note that the data also emphasize heterogeneity in response capacity – but not response type - of individual tumor fragments of a given tumor (**b**).

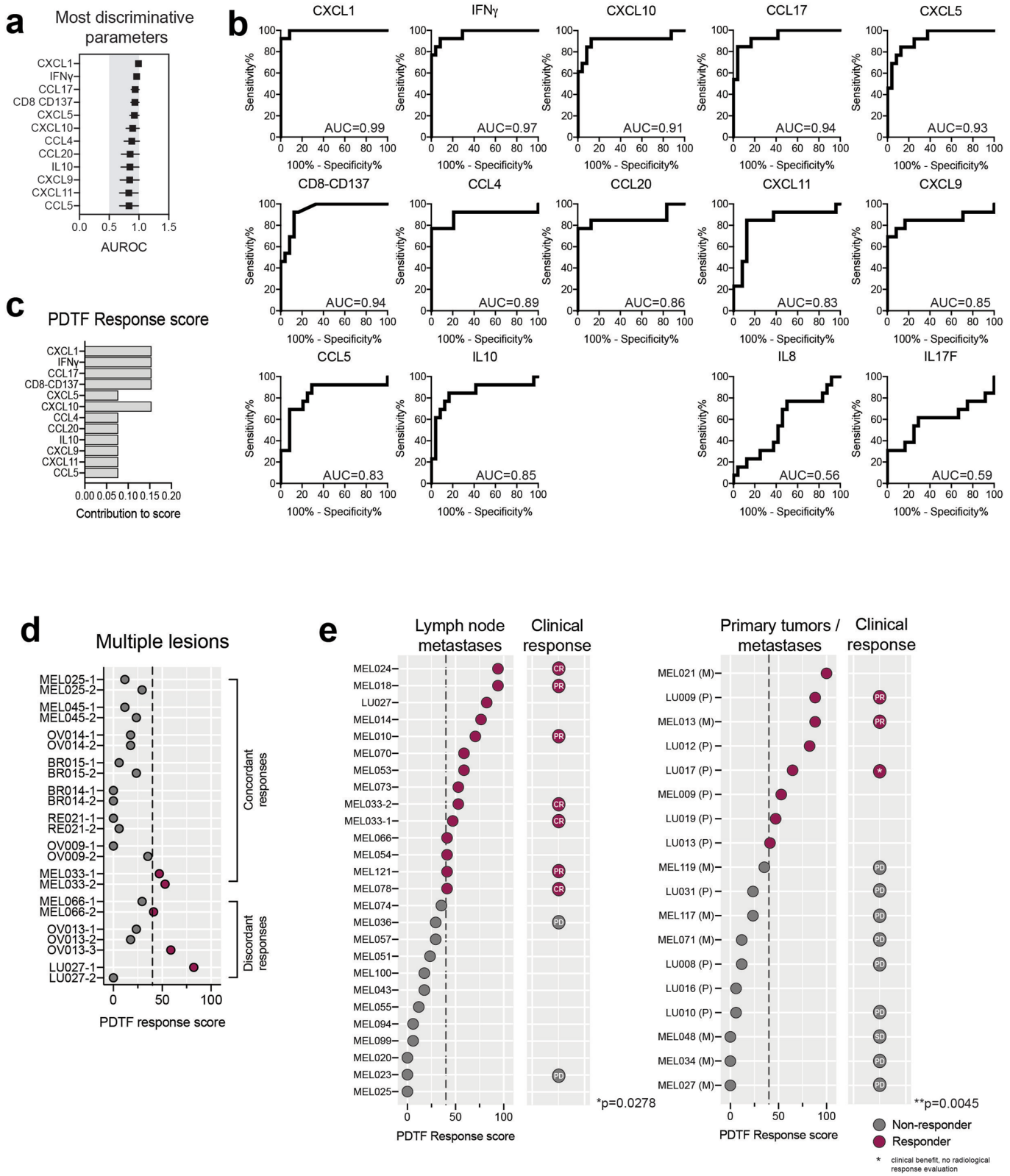

Extended Data Fig. 4 | Development of the PDTF response score. a, Potential of indicated markers defined by the area under the receiver operator curve (AUROC) to discriminate between anti-PD-1 responsive and non-responsive tumors. **b**, ROC curves of the 12 parameters selected for the score. As a comparison, plots for two parameters with no discriminative value (IL8 and IL17F) are depicted. **c**, Weighting of the twelve parameters used in the score. **d**, PDTF response scores for 11 tumors for which two or three lesions from distinct localizations were tested (Supplementary Table 3). Tumors with concordant (8/11) and discordant (3/11) responses are indicated. **e**, PDTF response score and matched clinical response for lesions derived from either lymph node metastases (left, n = 27) or primary tumors (P)/distant metastases (M) (right, n = 18). Significance was determined by Fisher's exact test.

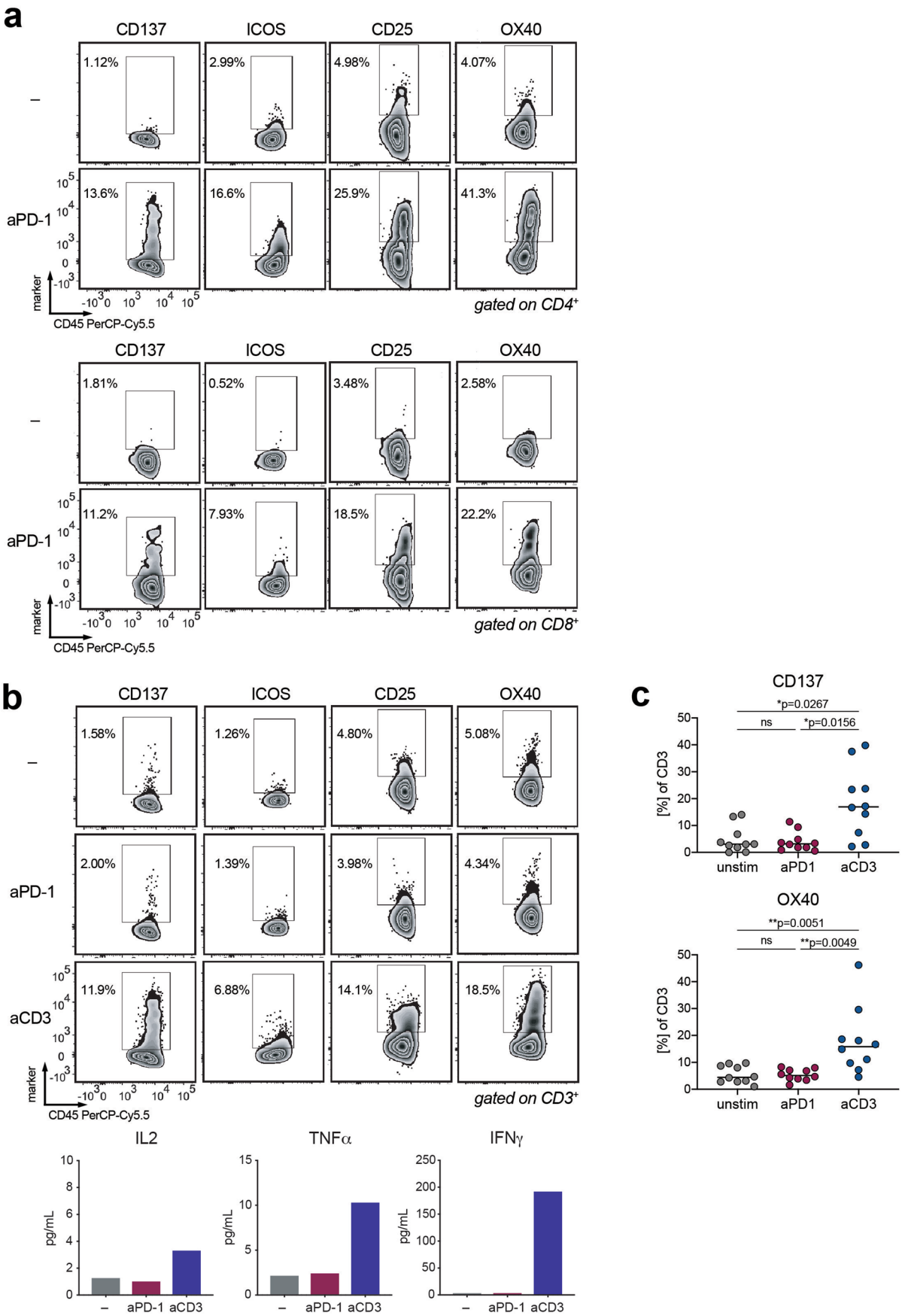

Extended Data Fig. 5 | See next page for caption.

Extended Data Fig. 5 | T cell activation upon ex vivo PD-1 blockade in PDTF-R and PDTF-NR tumors. a, Expression of T cell activation markers in $CD4^+$ T cells (top) and $CD8^+$ T cells (bottom) from untreated or anti-PD-1 treated PDTF cultures, as assessed by flow cytometry. Data are from the same responding tumor sample as in Fig. 2a (LU012). **b**, Expression of T cell activation markers in $CD3^+$ T cells and secretion of T cell effector cytokines in PDTFs that were either untreated, treated with PD-1 blockade, or treated with anti-CD3 antibodies, as assessed by flow cytometry and bead-based immunoassay, respectively. Data from a representative infiltrated non-responding tumor sample (LU010) are depicted. **c**, Quantification of CD137 and OX40 expression on $CD3^+$ T cells in PDTFs that were either untreated, treated with PD-1 blockade, or treated with anti-CD3 antibodies (n = 10 PDTF-NRs). $^*P < 0.05$, $^{**}P < 0.01$ by Kruskal-Wallis test corrected for multiple comparisons.

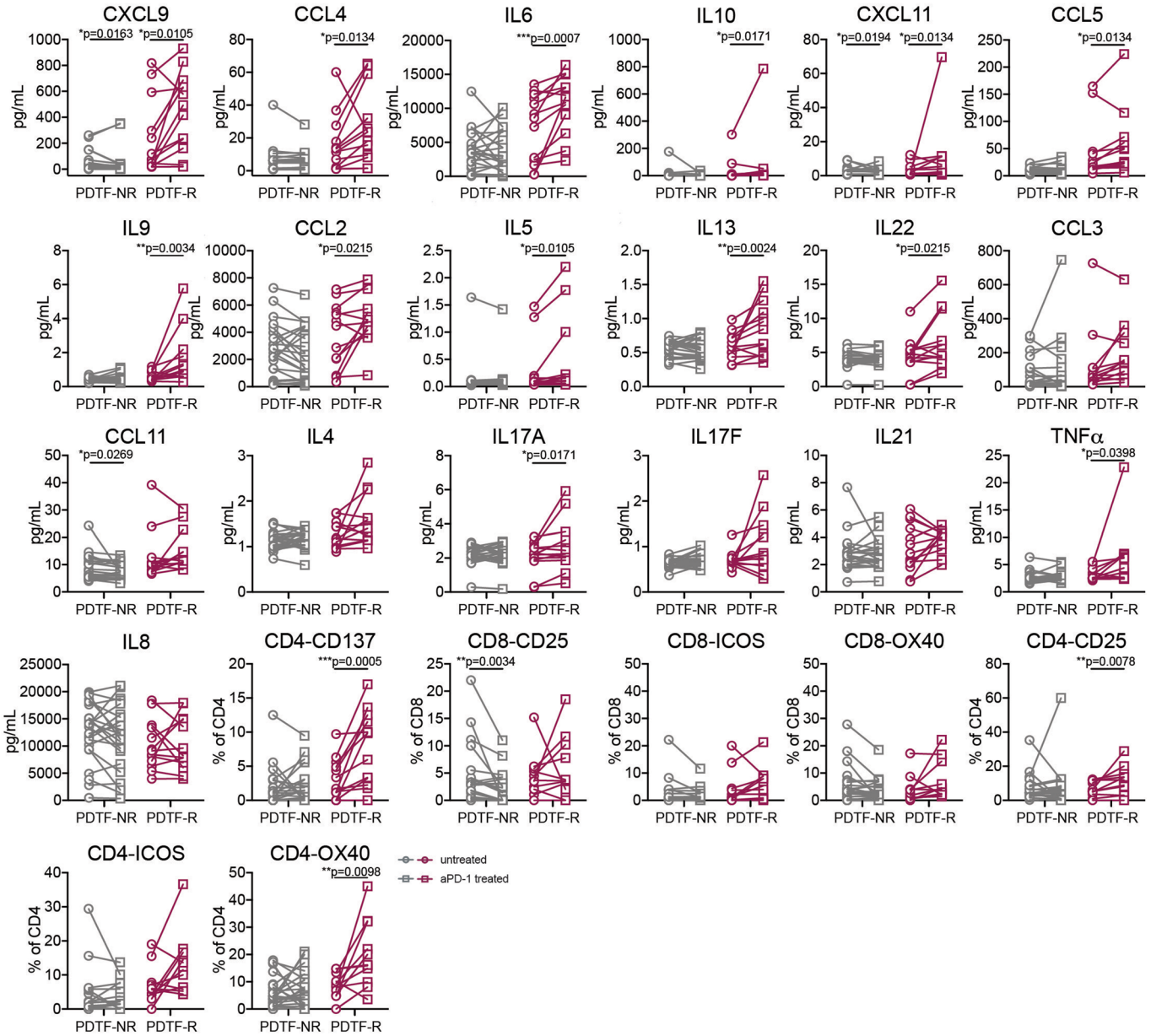

Extended Data Fig. 6 | Immunological responses upon ex vivo PD-1 blockade. Comparison of additional parameters assessed in untreated and anti-PD-1 treated PDTFs that are not depicted in Fig. 2c. Values are displayed separately for PDTF-R and PDTF-NR. *$P < 0.05$, **$P < 0.01$, ***$P < 0.001$ by two-tailed Wilcoxon test.

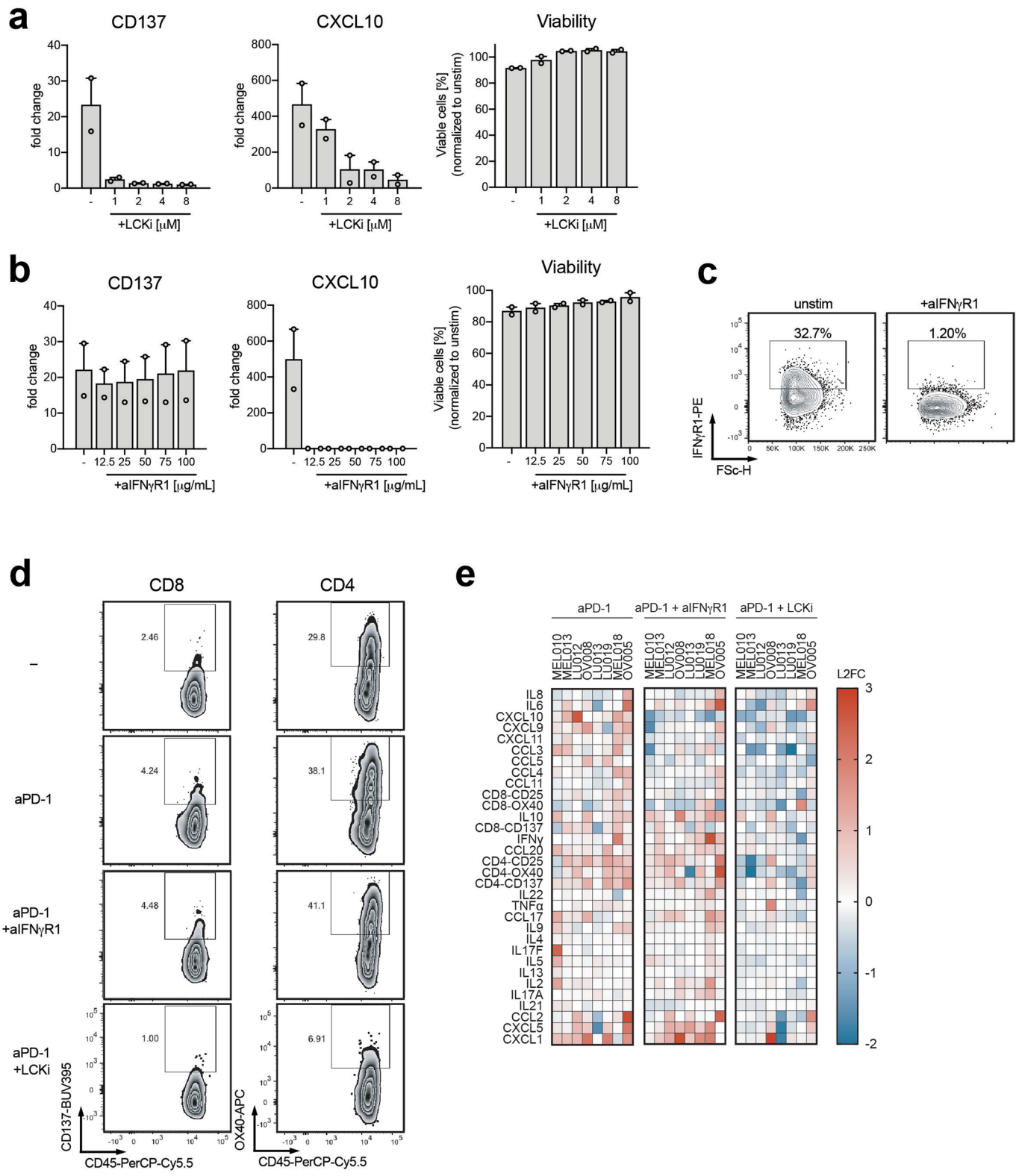

Extended Data Fig. 7 | See next page for caption.

Extended Data Fig. 7 | Modulation of the anti-PD-1 response by LCK inhibition or IFNγ receptor blockade. a-**b**, Titration of Lck inhibitor (LCKi) (**a**) and IFNγ receptor 1 blocking antibody (aIFNγR1) (**b**) in PBMCs stimulated with anti-CD3/anti-CD28 for 48 h. LCKi was added 2 h and aIFNγR1 1 h before PD-1 blockade at the indicated concentrations. The differential inhibition of CD137 expression on $CD3^+$ T cells and CXCL10 secretion reflect interference at the level of T cell activation (LCKi), or downstream, at the level of IFNγ-induced gene expression (aIFNγR1). Viability was comparable for both compounds and at all dosing levels. Shown are 2 independent experiments. Bars and error bars indicate mean + s.e.m. **c**, Flow plot depicting blockade of the IFNγR1 in the presence of aIFNγR1 during culture, as measured using a fluorescently labeled aIFNγR1 antibody that binds to the same epitope. **d**, Flow plots depicting activation of $CD8^+$ T cells, as measured by CD137 expression, and $CD4^+$ T cells, as measured by OX40 expression, in PDTFs that were either uncultured or treated with anti-PD-1, anti-PD-1+aIFNγR1 or anti-PD-1+LCKi for 48 h. One representative example of 8 PDTF cultures is depicted. **e**, T cell activation and cytokine/chemokine profiling of 8 PDTF-R tumors treated with anti-PD-1, anti-PD-1 + αIFNgR1, or anti-PD-1+LCKi for 48 h. Data are expressed as $\log_2$ fold change (L2FC) relative to the untreated condition.

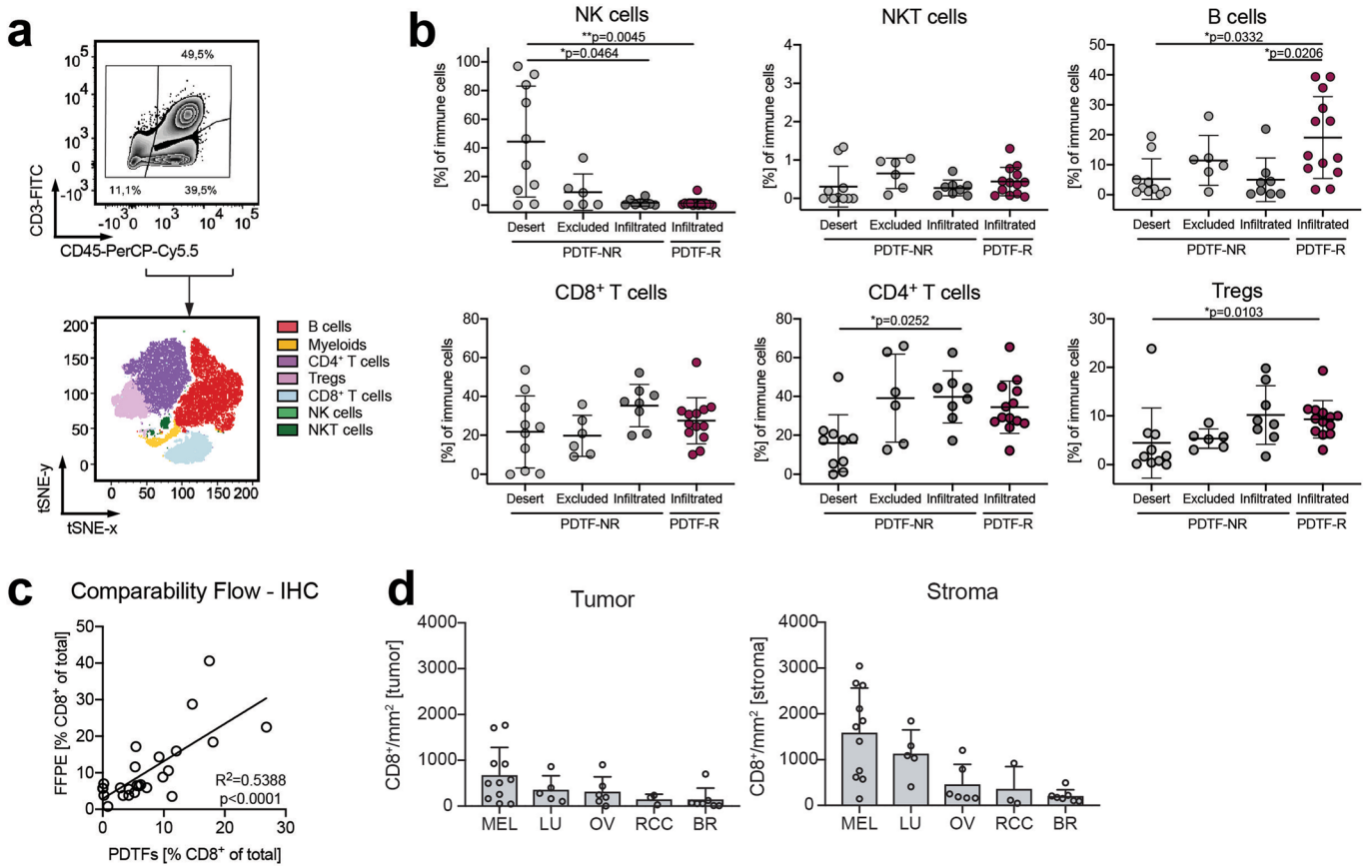

Extended Data Fig. 8 | Immune composition of PDTF-R and PDTF-NR tumors. a, Flow plots depicting the gating strategy and tSNE clustering of immune subsets. **b**, Quantification of indicated immune cell subsets within total immune cells (CD45$^+$) for the four distinct TME subtypes (desert, excluded, infiltrated non-responders, and infiltrated-responders, n = 37). Shown are mean +/- s.d., $^*P < 0.05$, $^{**}P < 0.01$ by Kruskal-Wallis test. **c**, Correlation between the percentage of CD8$^+$ T cells quantified by either flow cytometry or IHC in matched samples (n = 35). Significance was determined by linear regression analysis. **d**, Digital quantification of CD8$^+$ T cells in intratumoral and stromal regions displayed per tumor type (n = 35). Bars and error bars indicate mean + s.d..

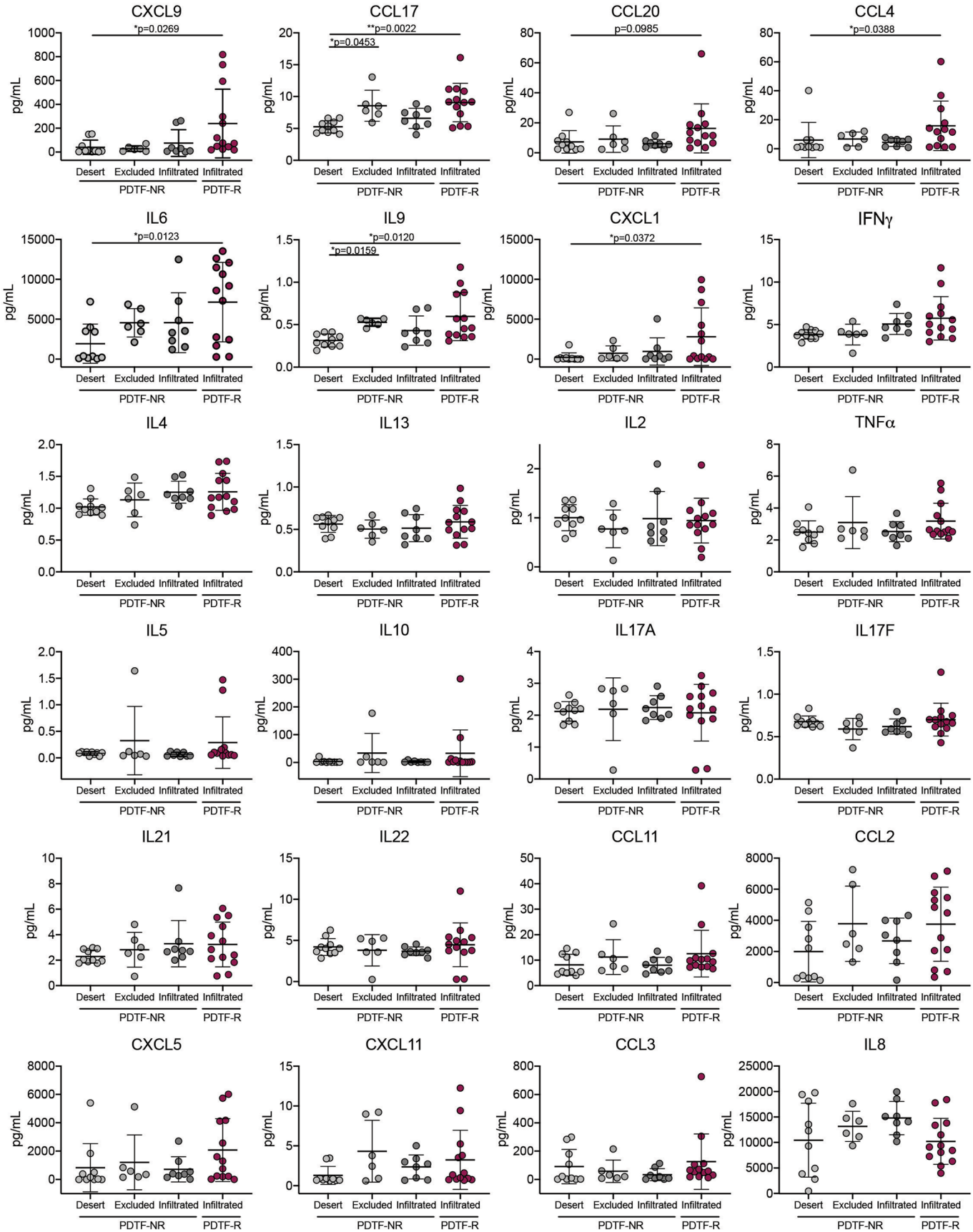

Extended Data Fig. 9 | Steady-state cytokine and chemokine profiles. Quantification of additional parameters assessed in untreated PDTFs after 48 h of culture (n = 37) that are not depicted in Fig. 3g. Values are displayed separately for desert, excluded, infiltrated PDTF-NR and infiltrated PDTF-R tumors. Shown are mean +/- s.d., $^{*}P < 0.05$, $^{**}P < 0.01$ by Kruskal-Wallis test corrected for multiple comparisons.

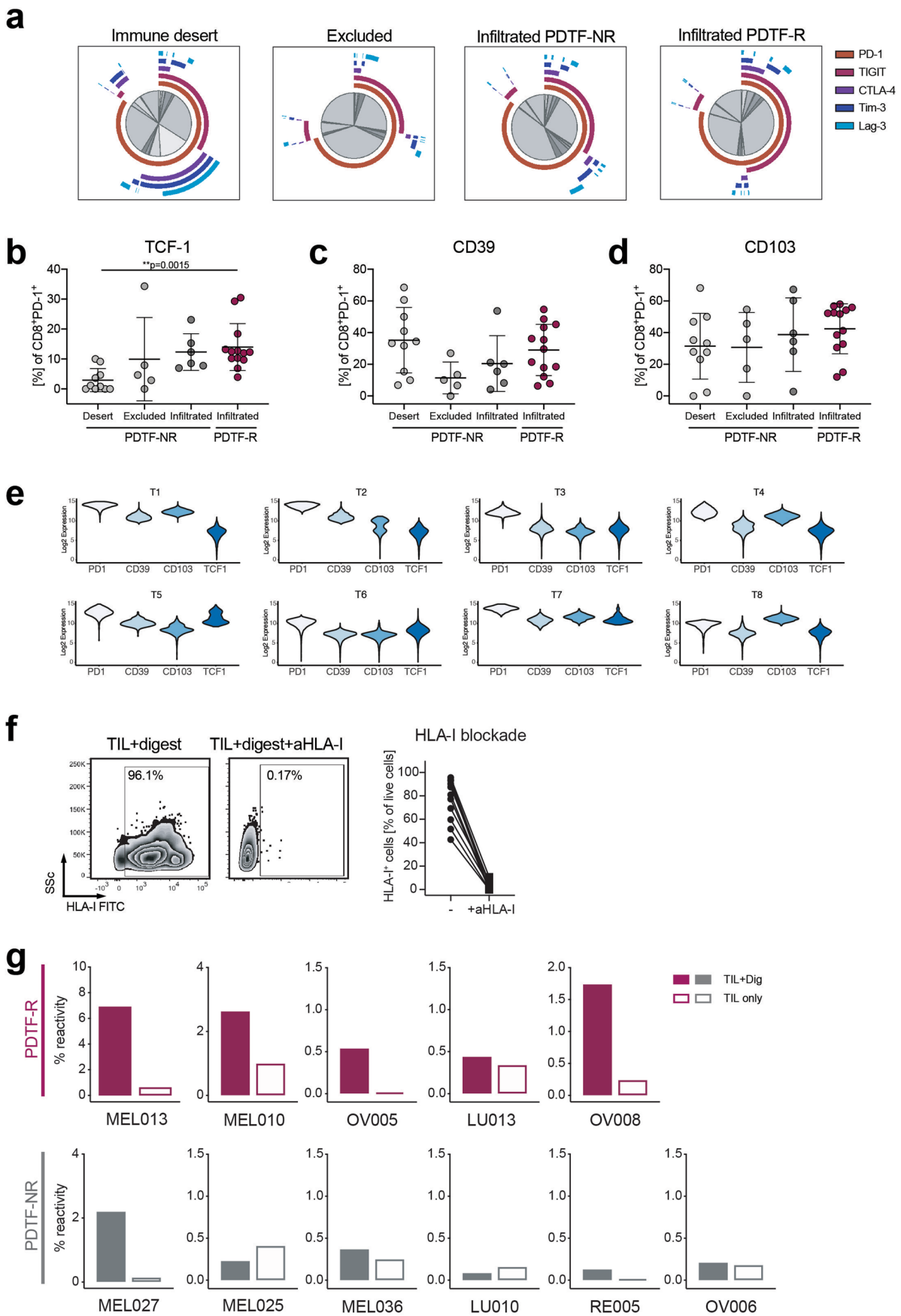

Extended Data Fig. 10 | See next page for caption.

Extended Data Fig. 10 | T cell differentiation states and tumor reactivity across distinct TME types. a, SPICE analysis[47] visualizing the co-expression of distinct immune checkpoints on $CD8^+$ T cells within the TME subtypes (as indicated by the pie arc). Means of all tumors per TME subtype (Desert, n = 10; Excluded, n = 5; Infiltrated PDTF-NR, n = 6; Infiltrated PDTF-R, n = 13) are depicted. **b-d**, Quantification of TCF-1, CD39, and CD103 expression on PD-1^+CD8^+ T cells by flow cytometry (n = 34). Shown are mean +/- s.d., $^{**}P < 0.01$ by Kruskal-Wallis test corrected for multiple comparisons. **e**, Violin plots showing the expression of PD-1, CD39, CD103, and TCF-1 in the clusters defined in Fig. 5a. **f**, Detection of HLA class-I on total live cells in the absence or presence of an HLA I blocking antibody. **g**, Tumor reactivity (measured as production of either IFNγ, TNFα, or both) within expanded $CD4^+$ T cells in the absence or presence of tumor digest for five PDTF-R and six PDTF-NR tumors.

nature research

Corresponding author(s): Daniela Thommen

Last updated by author(s): May 13, 2021

Reporting Summary

Nature Research wishes to improve the reproducibility of the work that we publish. This form provides structure for consistency and transparency in reporting. For further information on Nature Research policies, see Authors & Referees and the Editorial Policy Checklist.

Statistics

For all statistical analyses, confirm that the following items are present in the figure legend, table legend, main text, or Methods section.

n/a	Confirmed	
☐	☒	The exact sample size (*n*) for each experimental group/condition, given as a discrete number and unit of measurement
☐	☒	A statement on whether measurements were taken from distinct samples or whether the same sample was measured repeatedly
☐	☒	The statistical test(s) used AND whether they are one- or two-sided *Only common tests should be described solely by name; describe more complex techniques in the Methods section.*
☐	☒	A description of all covariates tested
☐	☒	A description of any assumptions or corrections, such as tests of normality and adjustment for multiple comparisons
☐	☒	A full description of the statistical parameters including central tendency (e.g. means) or other basic estimates (e.g. regression coefficient) AND variation (e.g. standard deviation) or associated estimates of uncertainty (e.g. confidence intervals)
☐	☒	For null hypothesis testing, the test statistic (e.g. *F*, *t*, *r*) with confidence intervals, effect sizes, degrees of freedom and *P* value noted *Give P values as exact values whenever suitable.*
☒	☐	For Bayesian analysis, information on the choice of priors and Markov chain Monte Carlo settings
☐	☒	For hierarchical and complex designs, identification of the appropriate level for tests and full reporting of outcomes
☐	☒	Estimates of effect sizes (e.g. Cohen's *d*, Pearson's *r*), indicating how they were calculated

Our web collection on statistics for biologists contains articles on many of the points above.

Software and code

Policy information about availability of computer code

Data collection	For flow cytometry data, FACS Diva Software version 8.0.1 (LSR II SORP BD), version 8.0.2 (Fortessa SORP BD) and version 8.5 (Symphony A5 SORP BD) were used. For cell sorting, FACS Diva Software version 8.0.1 (FACSAria Fusion SORP BD) was used. For histology data, slides were scanned using Aperio slide AT2 scanner (Leica Biosystems).
Data analysis	The following software was used in the study: FlowJo (v10.6.1), including UMAP plugin for data visualization and X-Shift plugin for myeloid cluster analysis. HALO digital image software version 2.3 (IndicaLabs): the HALO multiplex IHC version 1.2 base algorithm was adapted for CD8 analysis (counterstain, RGB 0.179,0.164,0.106; DAB, RGB 0.324,0.482,0.628). GraphPad Prism (v8.0e) Image J (v1.47) R software (v4.0.2) with base/standard packages

For manuscripts utilizing custom algorithms or software that are central to the research but not yet described in published literature, software must be made available to editors/reviewers. We strongly encourage code deposition in a community repository (e.g. GitHub). See the Nature Research guidelines for submitting code & software for further information.

Data

Policy information about availability of data

All manuscripts must include a data availability statement. This statement should provide the following information, where applicable:

- Accession codes, unique identifiers, or web links for publicly available datasets
- A list of figures that have associated raw data
- A description of any restrictions on data availability

All relevant flow, cytometry, immunohistochemistry, and cytokine/chemokine data are provided as Supplementary Data.

Field-specific reporting

Please select the one below that is the best fit for your research. If you are not sure, read the appropriate sections before making your selection.

☒ Life sciences ☐ Behavioural & social sciences ☐ Ecological, evolutionary & environmental sciences

For a reference copy of the document with all sections, see nature.com/documents/nr-reporting-summary-flat.pdf

Life sciences study design

All studies must disclose on these points even when the disclosure is negative.

Sample size	Sample size for each test is described in the manuscript and based on the availability of adequate patient samples for the analysis.
Data exclusions	For IHC analysis, 2 samples (BR015, LU008) were excluded, for T cell analysis, 3 samples were excluded (OV001, BR017, MEL020) and for myeloid cell analysis, 4 samples were excluded (OV001, BR017, MEL020, MEL014) because of material limitations.
Replication	Unless otherwise specified, experiments were performed without duplicates, because of material restrictions. Data describing reproducibility of cultures are provided in Fig. 2f, Extended data Fig.1d-e, Extended data Fig. 3a-d, and Supplementary Fig. 1.
Randomization	Randomization is not relevant for this study as tumor-specific properties were analyzed.
Blinding	All replicate experiments were performed blindly. Researchers were blinded during experiments to whether patients received anti-PD-1 therapy and the subsequent clinical outcome. Scoring of immunohistochemistry stainings was performed by pathologists blinded to the study conditions.

Reporting for specific materials, systems and methods

We require information from authors about some types of materials, experimental systems and methods used in many studies. Here, indicate whether each material, system or method listed is relevant to your study. If you are not sure if a list item applies to your research, read the appropriate section before selecting a response.

Materials & experimental systems

n/a	Involved in the study
☐	☒ Antibodies
☒	☐ Eukaryotic cell lines
☒	☐ Palaeontology
☒	☐ Animals and other organisms
☐	☒ Human research participants
☒	☐ Clinical data

Methods

n/a	Involved in the study
☒	☐ ChIP-seq
☐	☒ Flow cytometry
☒	☐ MRI-based neuroimaging

Antibodies

Antibodies used

Antibodies used for flow cytometry (clone, dilution, supplier-ID):
anti-PD-1 PE-Cy7 (clone: EH12.1, 1:20, cat# 561272); anti-CD137 PE (clone: 4B4-1, 1:20, cat# 555956); anti-CD137 BUV395 (clone: 4B4-1, 1:50, cat# 745737); anti-CD8 BUV563 (clone: RPA-T8, 1:50, cat# 565695); anti-CD3 BV711 (clone: UCHT1, 1:50, cat# 563725); anti-CD103 BV421 (clone: Ber-ACT8, 1:20, cat# 563882); anti-TNF-α PE-Cy7 (clone: MAb11, 1:50, cat# 557647); anti-CD11c PE-CF594 (clone: 3.9, 1:200, cat# 565920); anti-HLA-DR BUV395 (clone: L243af, 1:100, cat# 565972); anti-CD31 BV480 (clone: WM-59, 1:100, cat# 566144); anti-CD86 BUV563 (clone: FUN-1, 1:50, cat# 741386); all from BD Bioscience.
anti-CD3 FITC (clone: SK7, 1:50, cat# 344804); anti-CD8 BV605 (clone: RPA-T8, 1:100, cat# 301002); anti-CD4 BV421 (clone: SK3, 1:100, cat# 344632); anti-OX40 APC (clone: BerACT35, 1:20, cat# 350008); anti-CD25 AF700 (clone: BC96, 1:20, cat# 302622); anti-CD19 BV605 (clone: SJ25C1, 1:50, cat# 363002); anti-FoxP3 AF647 (clone: 259D, 1:50, cat# 320214); anti-CD11c PE (clone: Bu15, 1:50, cat# 337206); anti-CD16 Alexa 700 (clone: 3G8, 1:50, cat# 302026); anti-TIM-3 BV421 (clone: F38-2E2, 1:20, cat# 345008); anti-CD39 FITC (clone: A1, 1:20, cat# 328206); anti-TCF1 PE (clone: 7F11A10, 1:20, cat# 655208); anti-CD3 PE (clone: SK7, 1:50, cat# 344806); anti-CD19 APC (clone: SJ25C1, 1:50, cat# 363006); anti-CD56 APC (clone: HCD56, 1:20, cat# 318310); anti-CD16 APC (clone: 3G8, 1:50, cat# 302012); anti-CD11b APC (clone: ICRF44, 1:50, cat# 301310); anti-CD11c APC (clone: 3.9, 1:50, cat# 301614); anti-HLA ABC FITC (clone: W6/32, 1:50, cat# 311404); anti-IFN-γ APC (clone: 4S.B3, 1:50, cat# 502512); anti-human lineage cocktail CD3/CD19/CD20/CD56 APC (clones: UCHT1, HIB19, 2H7, 5.1H11, 1:50, cat# 363601); anti-CD11b BV605 (clone: ICRF44, 1:50, cat# 101237); anti-CD68 FITC (clone: Y1/82A, 1:50, cat# 333806); anti-CD206 PE-Cy7 (clone: 15-2, 1:20, cat# 321124); anti-CD14 AF700 (clone: M5E2, 1:200, cat# 301822); anti-CD123 BV421 (clone: 6H6, 1:100, cat# 306018); anti-PD-L1 BV650 (clone: 29E.2A3, 1:100, cat# 329740); all from Biolegend.
anti-CD45 PerCP Cy5.5 (clone: 2D1, 1:100, cat# 45-9459-42); anti-CD3 APC-eFluor780 (clone: SK7, 1:50, cat# 47-0036-42); anti-ICOS FITC (clone: ISA-3, 1:25, cat# 11-9948-42); anti-CTLA-4 FITC (clone: 14D3, 1:50, cat# 11-1529-42); anti-LAG3 APC (clone: 3DS223H, 1:20, cat# 17-2239-42); anti-TIGIT PE (clone: MBSA43, 1:20, cat# 12-9500-42); all from Invitrogen.
IFNγ R1 PE (clone: 92101, 1:25, cat# FAB673P); anti-Fap-alpha PE (clone: 427819, 1:20, cat# FAB3715P-100); all from R&D

systems.

Antibodies used for immunohistochemistry (clone, dilution, supplier-ID):
anti-CD8 (clone C8/144B, 1:200, cat# M7103); anti-CD20 (clone L26, 1:800, cat# M0755); both from DAKO/Agilent.
anti-CD21 (clone2G9, 1:500, cat# NCL-CD21-2G9) from Leica Biosystems.
anti-CD4 (clone SP35, 1:25, cat# 104R-15) from Cell Marque.
anti-CD3 (clone SP7, 1:100, cat# M3074) from Spring/ITK.
anti-PD-1 (clone NAT105, Ready-to-Use, cat# 760-4895) from Roche Diagnostics.

Validation

All antibodies are commercially available and were only used for applications validated by the manufacturer.
Antibodies for flow cytometry were validated and titrated by staining anti-CD3/-CD28 stimulated and unstimulated human PBMCs and/or human tumor tissue.
For immunohistochemistry stainings, CD3, CD8 and CD4 are diagnostic markers and PD-1, CD20 and CD21 were certified for research purposes. All antibodies were validated either on tonsil tissue and/or human diagnostic tissue by the local Pathology Department (NKI-AVL).

Human research participants

Policy information about studies involving human research participants

Population characteristics	Peripheral blood was obtained from healthy volunteers collected by Blood Bank Sanquin (Amsterdam, The Netherlands). Tumor samples were collected from individuals with melanoma, non-small cell lung cancer, breast cancer, ovarian cancer or renal cell carcinoma undergoing surgical treatment at the Netherlands Cancer Institute (NKI-AVL), The Netherlands. Detailed patient characteristics are described in Supplementary Tables 1-3.
Recruitment	All eligible patients undergoing surgery for cancer and without prior systemic treatment were offered to participate in the study. As entry in the study was based on either opt-out (until May 23, 2018) or active enrollment (after May 23, 2018), this could in theory as with any consent procedure influence the inclusion of patients.
Ethics oversight	The study was approved by the institutional review board of the NKI-AVL and performed in compliance with all relevant ethical regulations.

Note that full information on the approval of the study protocol must also be provided in the manuscript.

Flow Cytometry

Plots

Confirm that:

☒ The axis labels state the marker and fluorochrome used (e.g. CD4-FITC).

☒ The axis scales are clearly visible. Include numbers along axes only for bottom left plot of group (a 'group' is an analysis of identical markers).

☒ All plots are contour plots with outliers or pseudocolor plots.

☒ A numerical value for number of cells or percentage (with statistics) is provided.

Methodology

Sample preparation	Solid tumor lesions were macroscopically selected by a pathologist from the resected tumor material and part of the tumor was collected in ice-cold collection medium (RPMI 1640 medium (Thermo Fisher) supplemented with 2.5% fetal bovine serum (FBS, Sigma), 1% Penicillin-Streptomycin (Roche)) for subsequent PDTF cultures. A second part of the tumor was embedded in paraffin for histological analysis and for analysis of tumor cell content within the collected lesion. Tissue materials collected for subsequent PDTF cultures were immediately processed by manual cutting into small tumor fragments (PDTFs) of 1-2 mm3 size on ice. After processing, PDTFs from different tumor areas were mixed to ensure uniform representation of the tumor lesion, and were frozen in cryovials containing 1 ml FBS with 10% DMSO (Sigma) with 8-15 PDTFs per vial. All PDTFs were cryopreserved in liquid nitrogen until further usage.
Instrument	Standard flow cytometry was performed on BD LSR II SORP, BD Fortessa SORP and Symphony A5 SORP Cell analyzers (BD Biosciences). Sorting was performed on BD FACSAria Fusion SORP cell sorter (BD Biosciences).
Software	Data was collected using the BD FACS Diva Software version 8.0.1 (LSR II SORP; FACSAria Fusion SORP), version 8.0.2 (Fortessa SORP), version 8.5 (Symphony A5 SORP) and analyzed by FlowJo v10.6.1 (Tree Star Inc.).
Cell population abundance	Sorted intratumoral CD3 positive T cells had a post-sort purity > 98%.
Gating strategy	Sample 'clean-up' was performed by gating on time, exclusion of doublets in FSC-A/FSC-H and SSC-A/SSC-H plots and inclusion of live cells (IR Dye neg or Zombie UV neg). For T cell activation and T cell phenotyping, T cells were identified as CD45+/CD3+/CD8+ or CD45+/CD3+/CD4+. Pre-dysfunctional (TCF-1+) and dysfunctional (CD39+) populations were assessed in PD-1+CD8+ T cells. Immune composition of PDTFs was assessed by identification of T cells (CD45+CD3+), non-T cells (CD45+CD3-) and non-immune cells (CD45-CD3-). T cells were further subdivided in CD3+CD8+ T cells, CD3+CD4+ T cells, CD3+CD8-CD4-CD16+ NKT cells. Non-T

cells were further subdivided in CD3-CD19+ B cells, CD3-CD19-CD11b/CD11c-CD16+ NK cells and in CD3-CD19-CD11b/CD11c+CD16+, CD3-CD19-CD11b/CD11c+CD16-, CD3-CD19-CD11b/CD11c-CD16- myeloid cells.
For detailed myeloid cell composition of PDTFs, immune cells were identified (CD45+) and non-immune cells (CD45-). Within non-immune cells, endothelial cells were identified (CD31+) and fibroblast (FAP-alpha+). T cells, B cells and NK cells were identified (CD45+Lin+) and myeloid cells (CD45+Lin-). Subdivision of the myeloid compartment in clusters was defined based on the expression of CD11c, CD11b, CD68, CD206, CD14, CD123, CD86, HLA-DR and PD-L1.

For sorting, cells were gated on SSC-A/FSC-A, FSC-A/FSC-H for singlets and live cells (DAPI negative). T cells were identified as CD45 positive, bulk (CD19, CD56, CD16, CD11b, CD11c) negative and CD3 positive.

To evaluate reactivity of sorted CTV-labeled intratumoral T cells, data was first gated on singlets in FSC-A/FSC-H and SSC-A/SSC-H plots and IR Dye negative live cells. Sorted T cells were identified as either CD3+/CTV+/CD8+ or CD3+/CTV+/CD8-. IFNy and TNF were gated within CD8+ and CD8- subsets.

☒ Tick this box to confirm that a figure exemplifying the gating strategy is provided in the Supplementary Information.